Electrochemical Band-filling Control for Thin Films and Single Crystals of Porphyrazines

（ポルフィラジン薄膜および結晶における電気化学バンドフィリング制御）

MIYOSHI Yasuhito

三 吉　康 仁

Table of Contents

Chapter 1. General Introduction

1.1 Overview of Organic Conductors

Since the first highly conductive organic compound, perylene-bromine complex, was reported by Akamatsu, Inokuchi and Matsunaga in 1954,[1] a number of conductive or metallic charge transfer complexes have been prepared and their physical properties investigated.[2] Fig. 1.1 shows some of the components of organic conductors. An electron acceptor, 7,7,8,8-tetracyanoquinodimethane (TCNQ),[3] was synthesized in 1960 and an electron donor, tetrathiafulvalene (TTF),[4,5] was synthesized in 1970, followed by the discovery of the first organic metal, TTF·TCNQ, by Ferraris *et al*.[6,7] The first organic superconductor, $(TMTSF)_2PF_6$ (T_c = 0.9 K at 12 kbar), was also reported by Bechgaard *et al*. in 1980.[8]

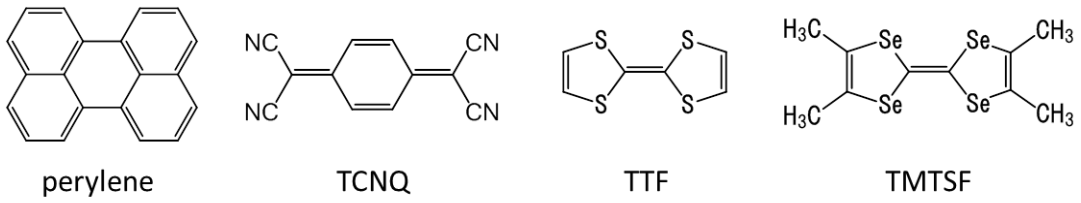

Figure 1.1 Molecular structures of selected organic conductors.

The methods used to generate organic conductors are to form a regular segregated stack of molecules and to obtain a partially-filled band caused by a partial charge transfer. Fig. 1.2 shows the band structure of a crystal composed of a one-dimensional regular stack of closed shell molecules. With the intermolecular

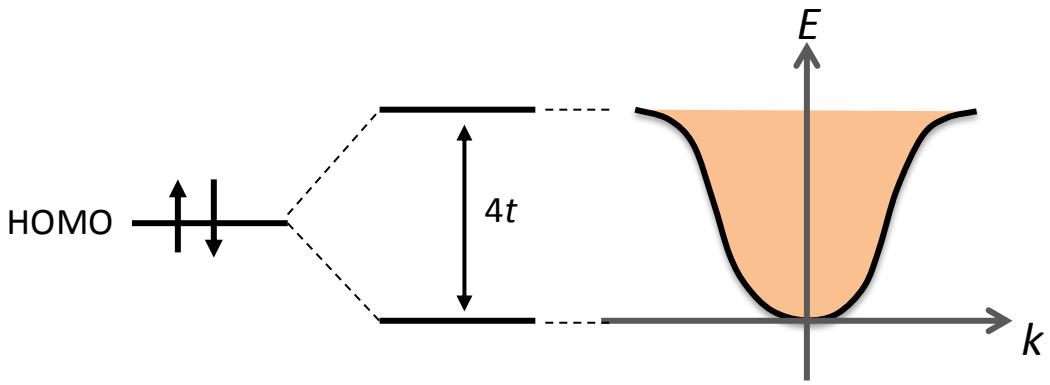

Figure 1.2 Band structure of the one-dimensional regular stack of closed shell molecules.

transfer integral *t*, a one-dimensional array of molecules forms the band from the corresponding HOMOs, the bandwidth of which is equal to 4*t*. Since the band is fully filled with electrons in the case of the closed shell system, this type of molecular solid is a band insulator. When molecules possess only one electron in the HOMO, such as in the case of a neutral radical, they should construct a half-filled band. A half-filled band is expected to be metallic according to a conventional band theory. In fact, however, neutral radicals do not show metallic behavior, but rather act as insulators or semiconductors.[9] To understand the electrical conductivities of solid materials, it is necessary to take into account the Coulomb repulsive force between electrons, namely electron correlation, which is ignored in a conventional band theory. This type of insulator caused by electron correlation is called a Mott insulator.[10–12] The electrons in a one-dimensional array of neutral radicals feel the Coulombic force *V* from electrons at neighboring sites (Fig. 1.3). For electrons in solid of neutral radicals, the extra energy $\varepsilon_g = U_{eff} - 4t$, where ε_g and U_{eff} are the energy gap and the on-site Coulomb repulsive energy, respectively, is required to transfer into the neighboring sites beyond the

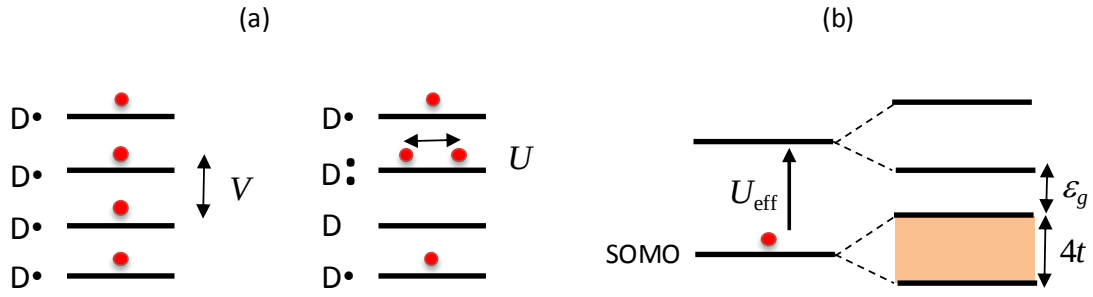

Figure 1.3 Coulombic repulsion energies of electrons on the neighboring SOMOs (*V*, left), and on the same SOMO (*U*, right). (b) Band structure of a crystal composed of neutral radicals, where the band gap (ε_g) = $U_{\mathrm{eff}} - 4t$.

repulsive energy. Therefore, to attain an organic conductor, the bandwidth *W* (= 4*t* in a one-dimensional system) should be larger than U_{eff}. This is one of the Mott criteria. The bandwidth increases by an enlarged transfer integral, and *U* decreases by the removal of electrons from a band. BEDT-TTF (abbreviated as ET) is one of the most studied donor molecules in charge transfer complexes.[13]

Fig. 1.4 shows a phase diagram for $(ET)_2X$ salts proposed by Kanoda.[14,15] In the $(ET)_2X$ complex, the ET molecule with a +0.5 charge forms a dimer, and each dimer has a hole. This strongly correlated system shows a variety of attractive physical properties, such as Mott insulator, metal, and superconductivity properties. The conductive properties are controlled by tuning the bandwidth through the chemical pressure effect in the present system, where the reduction of unit cell volume is caused by chemical substitutions. Thus, it is important to tune the bandwidth to investigate itinerant electron properties or localized electron magnetism of solid materials. Physical properties of solids are also expected to be controlled by tuning the degree of band-filling which is relevant to the modulation of *U*, although the band-filling control

has been difficult to realize at the experimental level.

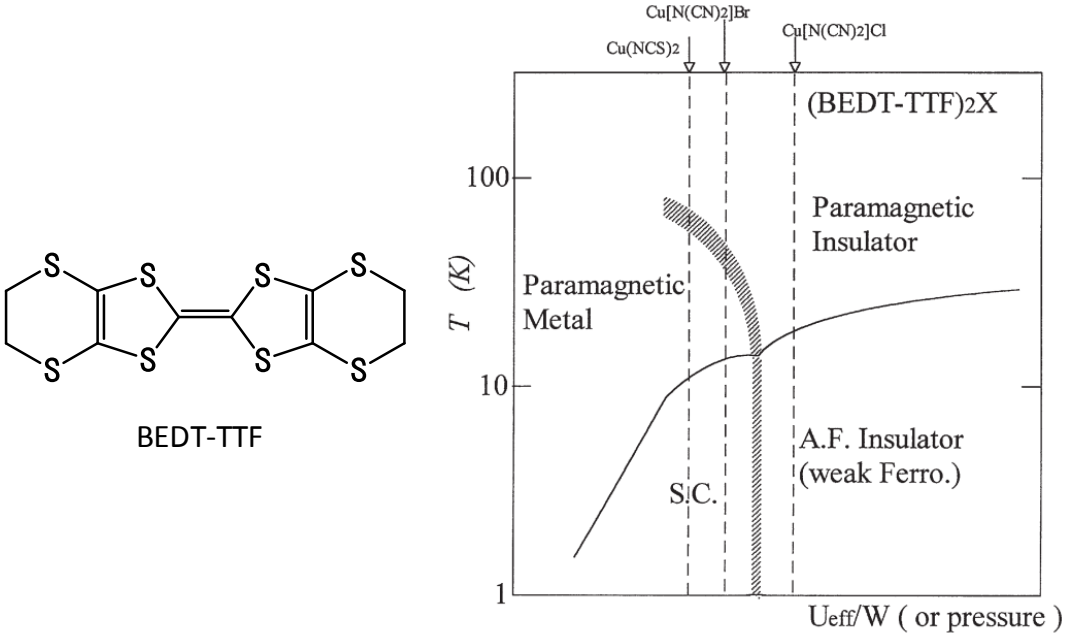

Figure 1.4 Molecular structure of BEDT-TTF (left) and phase diagram of $(BEDT\text{-}TTF)_2X$ by Kanoda.[14]

1.2 Band-filling Control in Organic Conductors

As described above, both band-filling control and bandwidth control are important techniques to control the physical properties of materials such as insulators, semiconductors, metals, or superconductors. The most difficult point in band-filling control for organic conductors is to maintain the crystal structure unchanged during the change of carrier density. The crystal structure is directly linked with the band structure, so that the changes in crystal structure cause a deformation of the original band structure. This is the reason why only a very limited number of studies have reported a successful band-filling control, although there have been a large number of studies concerning the control of carrier densities by means of chemical or physical doping. As shown in Fig. 1.5, there are four representative types of band-filling control. Each method is explained

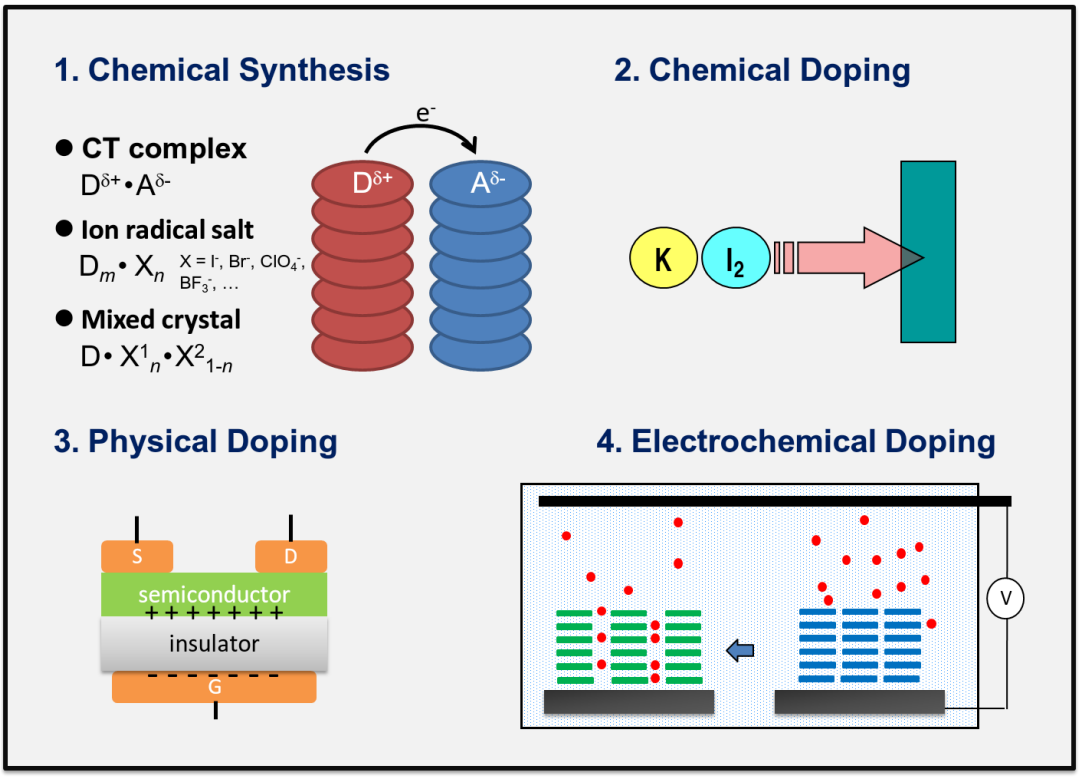

Figure 1.5 Strategies of the four representative types of band-filling control.

as follows.

1.2.1 Chemical Synthesis

Chemical synthesis is the most studied method for modulating the carrier density in a band of intermolecular compounds. The advantages of this method are its simple synthesis and higher crystallinity compared to chemical doping techniques.

The band structure in a 1:1 complex of donor and acceptor molecules ($D^{\delta+}A^{\delta-}$) depends on the degree of a charge transfer, δ. A complex with $\delta = 0$ is a neutral complex in which an HOMO band is fully occupied with electrons and a LUMO band is completely vacant, and thus it is a band insulator. A complex with $\delta = 1$ is a fully ionic complex which could give a conductive half-filled band in a classical band theory, although it is actually an ionic Mott insulator due to the electron correlation. In a partial CT complex, the degree of charge transfer is $0 < \delta < 1$, and the band-filling will be $\delta/2$. The degree of the charge transfer is determined by a balance between the electron-donating ability of donor molecules (the ionization energy of the donor: I_D) and the electron-accepting ability of acceptor molecules (the electron affinity of the acceptor: E_A).

There have been a few reports in which band-filling control was achieved by changing the fraction of donor or acceptor molecules in an isomorphous CT complex. To obtain an isomorphous structure, cations or anions with a similar size and different charges are required. Based on this idea, there have been several reports on successful band-filling control. For example, Fig. 1.6 shows a system of N-methylphenazinium (NMP) and phenazine with a similar molecular structure. Miller and Epstein reported that NMP in a [NMP][TCNQ] complex can be replaced with phenazine, resulting in a

composition of $[NMP]_{1-x}[phenazine]_x[TCNQ]$ ($0 \leq x \leq 0.5$).[16,17] Since the size and shape of phenazine are similar to those of NMP, 50% of NMP can be replaced with phenazine, maintaining the isostructure. As a result, their physical properties can be studied systematically based on the effect of band-filling without the structural changes that are usually caused by a molecular replacement. By replacing NMP with phenazine, the conduction electrons are removed from both molecular stacks to form a metallic band (Fig. 1.6).

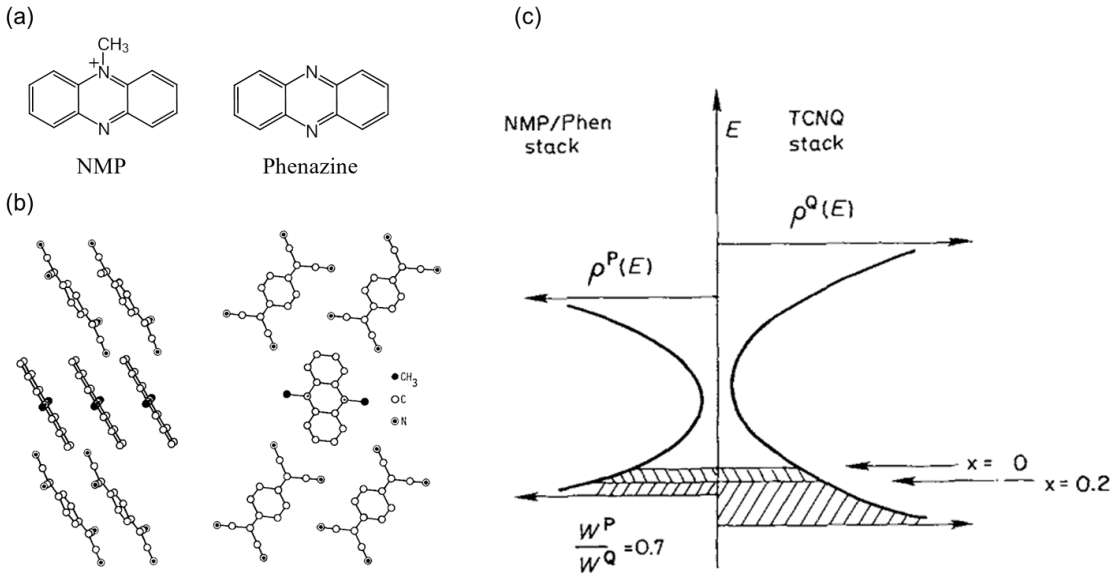

Figure 1.6 (a) Molecular structure of NMP and phenazine. (b) Crystal structure of [NMP][TCNQ]. (c) Band dispersion of the NMP/phenazine stack (left) and TCNQ stack (right) by Miller and Epstein.[16]

Ionic salts, D^+X^- consisting of a 1:1 complex, are Mott insulators when each molecule forms a segregated column with a regular stack. To tune the band-filling, it is required that the ratio of D to X is not 1:1. Although a number of DA complexes with DA ratios such as 1:2, 2:1, 2:3, 3:2, etc., have been synthesized,[18–22] systematic control of the stoichiometry has not been achieved. It is well known that such complexes

exhibit different crystal structures depending on the stoichiometry.[23,24]

1.2.2 Chemical Doping

Halogen and alkaline metal doping have been utilized as methods of chemical doping. So far, various A_3C_{60} compounds (A = Na,[25] K,[26,27] Rb,[28] etc.; Fig. 1.7) have been prepared by a direct reaction of alkaline metals with a parent C_{60} molecule. For example, Rb_2CsC_{60} exhibited a superconducting behavior below *ca.* 33K,[30] which is the highest critical temperature of organic superconductors under an ambient pressure. In an attempt to control the degree of band-filling in an A_3C_{60} system, various superconductors have been used. Fig. 1.7(b) shows a T_c plot as a function of carrier concentrations (n) in an A_3C_{60} system where T_c varies monotonically as the lattice constant of A_3C_{60} increases. This behavior was interpreted by a BCS mechanism, where

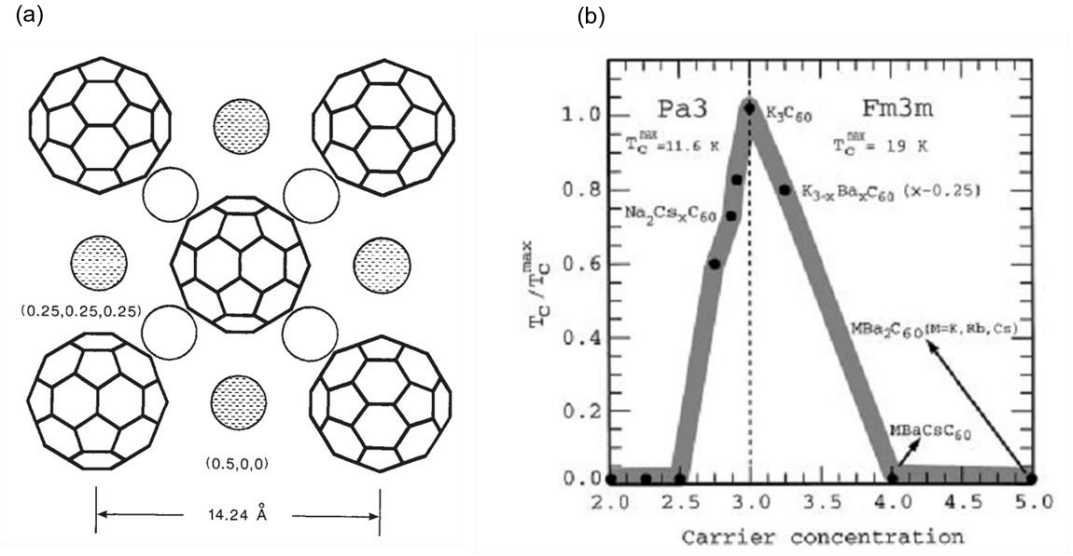

Figure 1.7 (a) Structure of K_3C_{60} by Stephenes *et al.*[27] The open and hatched spheres represent the potassium at the tetrahedral and octahedral sites, respectively. (b) A plot of T_c/T_c^{max} vs. carrier concentration in A_3C_{60} superconductors by Yildirim *et al.*[29]

higher T_c is expected by an increase of density of state at the Fermi energy due to the bandwidth narrowing as the lattice constant increases. In Fig. 1.7(b), T_c increases as the carrier concentration of C_{60} increases up to C_{60}^{3-} (n = 3), while T_c decreases with further electron doping into LUMOs. The peak of T_c at the carrier concentration n = 3 was explained by an orientational order effect.[31] The band-filling control was also achieved in $Na_2Cs_xC_{60}$ ($0 \leq x \leq 1$) and $K_{3-x}Ba_xC_{60}$ ($0 \leq x \leq 1$) systems.[29]

Although systematic band-filling control has been realized in A_3C_{60} systems, the crystal structure doped with alkaline metal or halogen ions exhibits significant structural defects and changes from its original crystal structure.

1.2.3 Physical Doping

Physical doping has the advantages that it maintains the crystal structures during the doping processes, unlike most chemical doping methods. The field effect doping is a representative physical doping method that utilizes an electric field to induce carriers into the sample. Fig. 1.8 depicts the device structure of the field effect transistor (FET). The FET consists of a metal electrode, an insulator layer, and inorganic/organic semiconductors from the bottom to the top. By applying the gate voltage (V_G) between the gate and source/drain electrodes, charge carriers are injected into the interface

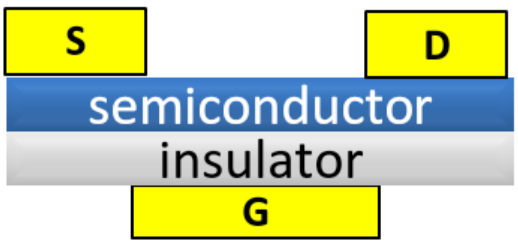

Figure 1.8 Schematic device structure of the field effect transistor.

between an insulator and a semiconductor. The induced carrier density increases proportionally to V_G, as explained by a conventional capacitor ($Q = CV$), and the maximum carrier density is determined by the capacitance of the insulator layer, C. The typical carrier density achieved in a conventional FET with an oxide insulator is less than 10^{13} cm^{-2}.[32] It is not large enough to induce a dramatic change in the physical properties, such as the superconducting transition, since the surface density of molecules is higher by several orders of magnitude than that of carriers injected by an electric field. Recently, Panzer and Frisbie *et al*. reported that organic polymer electrolytes utilized as an insulator layer of FET can accumulate an extremely large surface density of carriers as high as 10^{15} cm^{-2} due to the large capacitance of the electrical double layer.[33–36] Although the carrier density can be controlled readily by a field effect, the maximum carrier density still seems rather low for controlling the physical properties of organic materials.[37,38]

1.2.4 Electrochemical Doping

The electrochemical doping technique has been developed for conductive organic polymers such as polyacetylene,[39] polythiophene,[40] and polyaniline.[41] This is a technique to dope counter cations or anions into semiconductors in the solution containing their corresponding electrolytes. By oxidizing polymers electrochemically (*p*-doping), electrons are removed from their HOMOs with simultaneous doping of electrolyte cations into polymer matrix. On the other hand, by reducing the polymer (*n*-doping), electrons are injected into their LUMOs with anions insertion. In these processes, the degree of doping can be precisely controlled by tuning the electrode potential based on Nernst equation. The thermodynamic control of the doping

concentration under electrochemical equilibrium conditions is a significant advantage of electrochemical doping, which enables a more reproducible and widely tunable band-filling control compared to a conventional chemical doping.

Despite such important advantages, electrochemical doping has not been a popular method for molecular materials, unlike in conductive polymer systems. So far, there have been only a limited number of studies on electrochemical doping of organic small molecules,[42–45] since they are highly soluble to common organic or aqueous electrolyte solution compared to the low solubility of organic polymers. The most crucial disadvantage for applying this technique to molecular solids is that counter cations or anions penetrating into the molecular assembly to maintain a charge balance can cause a collapse of the crystal structures.[46]

Marks *et al*. reported that the cofacially joined phthalocyanine polymer $\{[Si(Pc)O]X_y\}_n$ ($X = BF_4^-$, TOS^-, SO_4^{2-}, etc.; Fig. 1.9, 1.10) exhibited a widely tunable band-filling control while maintaining the crystal structure.[47–49] The controlled-potential coulometry and electrochemical potential spectroscopy were applied to rapidly stirred slurries (Fig. 1.9 (a)) or to microcompactions of the solid phthalocyanine polymer

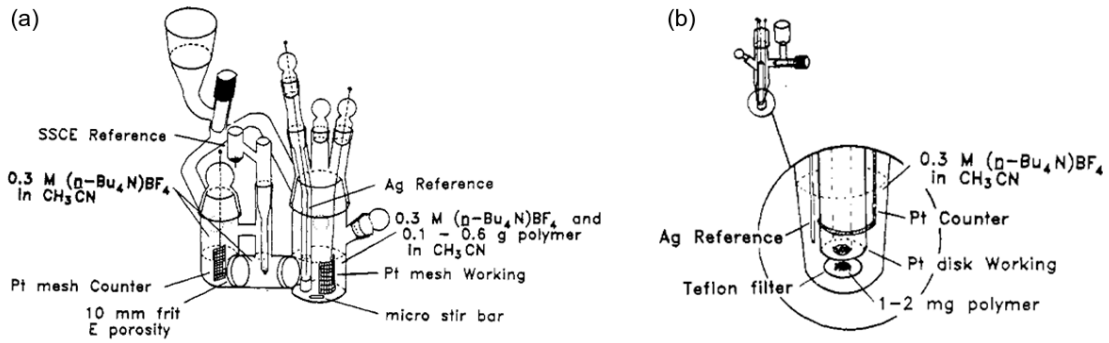

Figure 1.9 Schematic diagrams of electrochemical cells for (a) slurry doping experiments and (b) microcompaction doping experiments by Marks *et al*.[48]

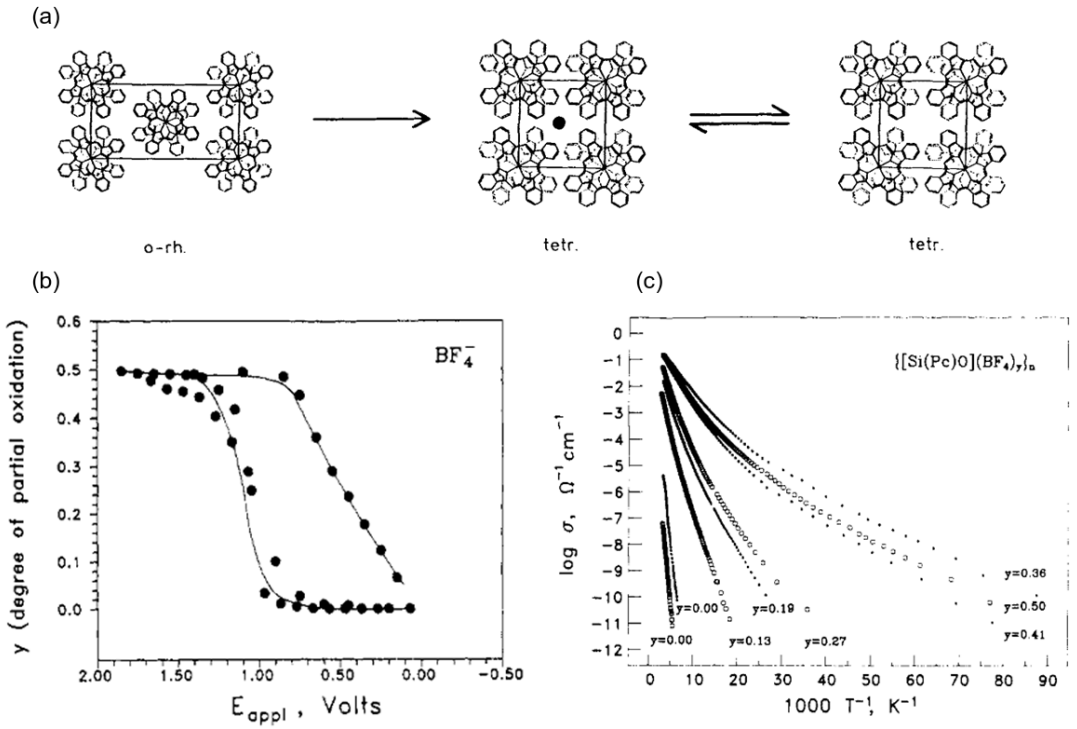

Figure 1.10 (a) Structural model of the changes accompanying electrochemical doping of $[Si(Pc)O]_n$, followed by thermal undoping. (b) A plot of the degree of partial oxidation (y) for slurry doping of $[Si(Pc)O]_n$ in (n-Bu_4N^+)BF_4^-/acetonitrile. (c) Temperature dependence of the electrical conductivity for $\{[Si(Pc)O(BF_4)_y]\}_n$ at various doping levels by Marks *et al*.[48,49]

$\{[Si(Pc)O]X_y\}_n$ (Fig. 1.9 (b)). For X = BF_4^-, the oxidation to $\{[Si(Pc)O](BF_4)_y\}_n$ ($0 \leq y \leq 0.5$) was accompanied with the structural transformation from the original orthorhombic to tetragonal phase (Fig. 1.10). After this transformation in the beginning process, all of the oxidized $\{[Si(Pc)O](BF_4)_y\}_n$ belonged to the isomorphous tetragonal phase. Therefore, it is possible to discuss the physical properties in relation to the degree of band-filling among isostructural products.

1.3 Structure and Properties of Porphyrazines

The synthesis and physical properties of porphyrazine compounds, including porphyrins, phthalocyanines (Pcs), and related derivatives (Fig. 1.11), have been extensively studied since the early 20th century due to their excellent optical and electrical characteristics and their chemical stability.[50] In recent decades, increasing attention has been paid to the utilization of functional porphyrazines in organic electronics such as photovoltaic cells,[51] thin film transistors,[52] and electroluminescence devices.[53] In these applications, the transport properties of the carrier have a major influence on the performance of the electronic devices. The carrier transport properties of porphyrazines have also been studied from the viewpoint of the fundamental relationship between their crystal structures and electrical conductivities.[50,54] A variety of conductors consist of phthalocyanines or porphyrins themselves, and intermolecular charge transfer complexes based on porphyrazines as a building block have been synthesized so far. The first Pc conductors were prepared in a study in 1977,[55] in which

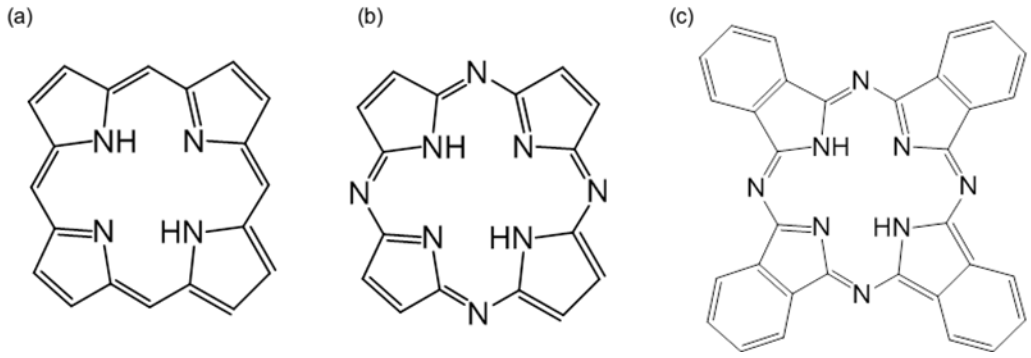

Figure 1.11 Molecular structures of (a) porphyrin, (b) porphyrazine, and (c) phthalocyanine.

highly conducting black powder was obtained when MPc (M = Fe, Co, Ni, Cu, Zn, Pt, H_2) was oxidized with iodine, followed by a report on a single crystal of NiPcI in 1978.[56] The crystal system is tetragonal with a space group *P*4/*mcc*, as shown in Fig. 1.12. NiPc is planar and stacks along the *c* axis, forming a one-dimensional column. Iodine atoms aligned in the channel along the *c* axis were assigned as I_3^-. Therefore, the actual charge distribution in this complex is $(NiPc)^{0.33+}(I_3^-)_{0.33}$, resulting in the construction of a 5/6 filled metallic one-dimensional band. Such a one-dimensional column structure is typical in the assembly of porphyrazines due to the π–π interactions. These π–π interactions facilitate molecular stacks in the direction that is perpendicular to molecular planes and construct one-dimensional columns. The interaction between these columns is very small compared to the π–π interaction within the column, and thus the charge transfer between columns is weak.

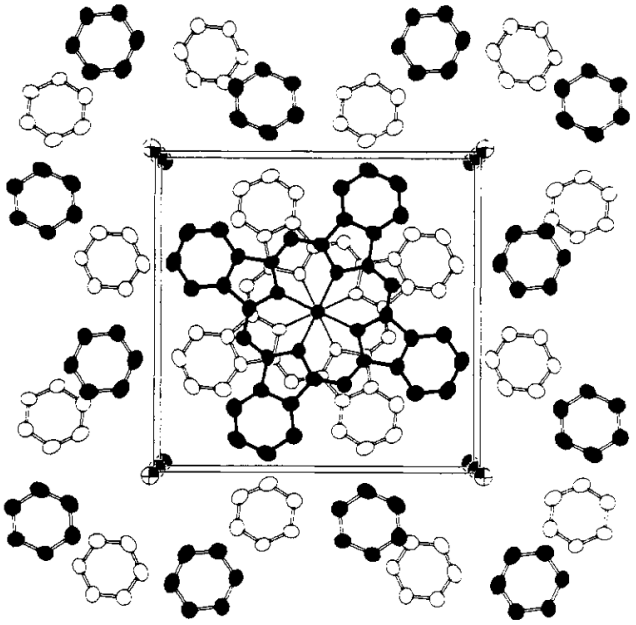

Figure 1.12 Crystal structure of NiPcI viewed parallel to the stacking direction by Marks *et al*.[57] Space group *P*4/*mcc*, *Z* = 2, *a* = 13.936 (6) Å, *c* = 6.488 (3) Å.

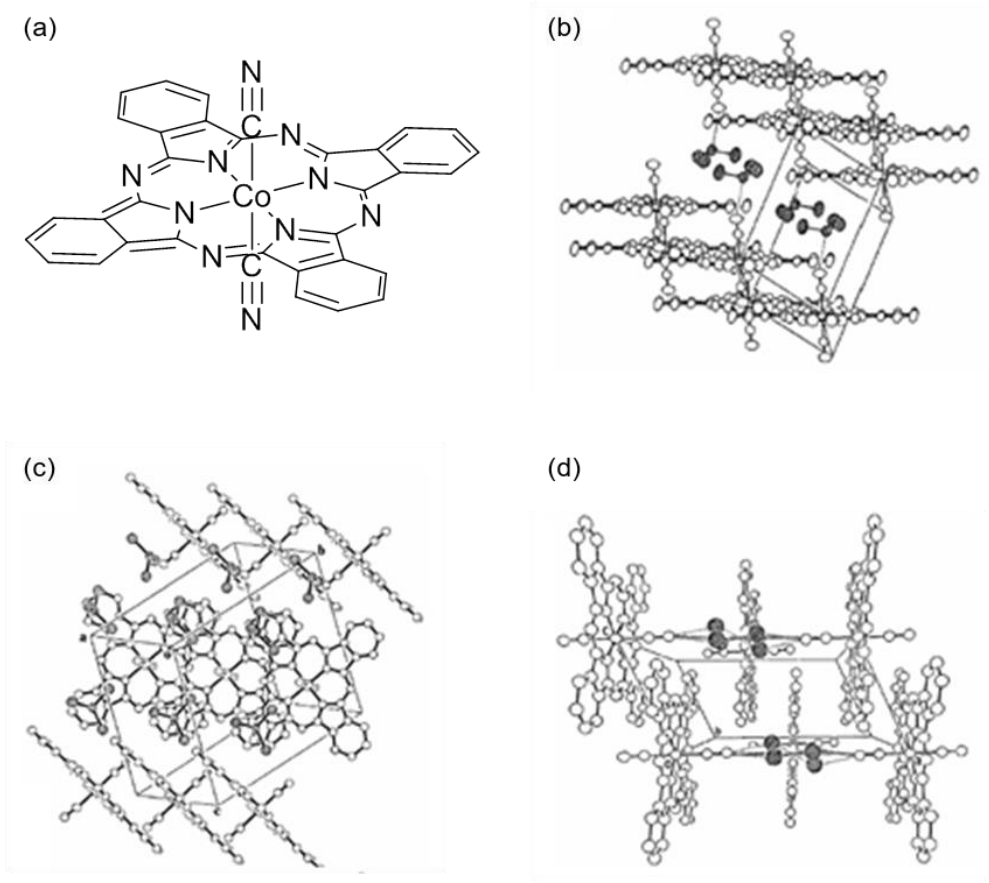

Figure 1.13 (a) Molecular structure of $Co(Pc)(CN)_2$. Crystal structures of $Co(Pc)(CN)_2$(solvent) by Inabe *et al.*,[59] where solvents are (b) $2CHCl_3$, (c) $2CHBr_3$, and (d) $2H_2O$, respectively.

To enhance interactions between porphyrazines in a lateral direction, Inabe *et al.* introduced axial ligands into a central metal (Fig. 1.13(a)). The crystals of $Co(Pc)(CN_2)$(solvent), which contained two axial CN ligands, were prepared by electrocrystallization.[58,59] Fig. 1.13 shows the crystal structure of axially substituted phthalocyanine complexes where the crystal structure changes depending on the solvents incorporated in the crystal structure. The crystal structure of these complexes revealed that the usual one-dimensional columnar structure cannot be formed because of the steric hindrance of axial ligands. Instead, the crystal containing chloroform has

two-dimensional sheets of slip-stacked phthalocyanines, and that containing water has a three-dimensional network of phthalocyanines. The electrical resistivity of $Co(Pc)(CN)_2 \cdot 2H_2O$ (Fig. 1.13 (d), 5 Ω cm in the compressed sample) is remarkably low as a neutral radical crystal. As described above, the physical properties of porphyrazines vary according to the structure of the ligands and central metal. Therefore, various functionalities can be produced by controlling these parameters. Among the various porphyrazines, two compounds with peculiar crystal structures and physical properties, namely tetrakis(thiadiazole)porphyrazine and lithium phthalocyanine, were used for electrochemical doping in this thesis.

1.3.1 Tetrakis(thiadiazole)porphyrazine

Numerous attempts have been made to modulate intermolecular interactions in the solid state of organic conductors, as mentioned above. For the purpose of obtaining two- or three-dimensional intermolecular interactions, the introduction of intermolecular interactions via the modification of molecular structures with chalcogen atoms has been shown to be effective.[60] The intermolecular interaction between columns achieved through chalcogen atoms at bridging sites increases intermolecular interactions by S···S, Se···Se, Te···Te contacts.

Based on this idea, the introduction of chalcogen atoms into a porphyrazine frame to overcome a low-dimensional structure was demonstrated by several groups. In 1998, Ercolani *et al*. synthesized tetrakis(thiadiazole)porphyrazine (H_2TTDPz; Fig. 1.14(a))[61] and the corresponding metallo-derivatives, MTTDPz (M = Mg, Mn,, Fe, Co, Ni, Cu, Zn, etc.),[62] in which intermolecular contacts of the thiadiazole rings were strongly expected in the solid state (Fig. 1.14(b)). However, the crystal structures had

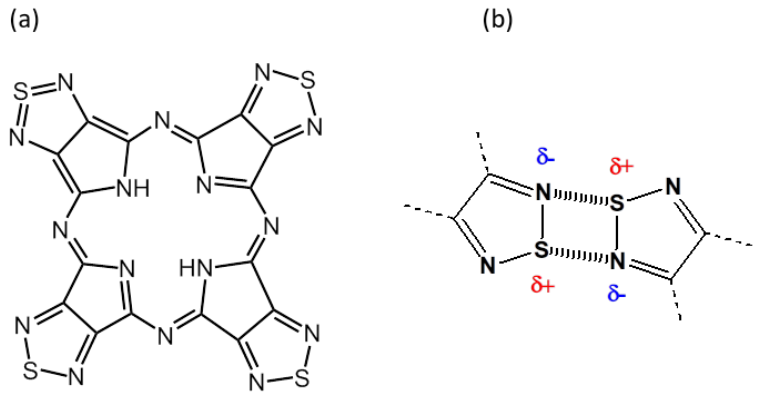

Figure 1.14. (a) Molecular structure of tetrakis(thiadiazole)porphyrazine (H_2TTDPz). (b) Schematic illustration of intermolecular interactions between thiadiazole rings caused by an electrostatic polarization, $N^{\delta-}$ and $S^{\delta+}$.

remained unidentified since the quality of crystals was not good enough to enable X-ray structural analysis. Fujimori and Suzuki *et al*. carried out the crystal growths, structural analysis and magnetic measurements on a series of MTTDPz in 2003.[63,64] The crystal structures of MTTDPz can be classified into three forms, α, β, and γ, and their structures depend significantly on the central metal ion (Table 1.1 and Fig. 1.15). The crystal structure of one of these compounds, H_2TTDPz, was found to consist of a two-dimensional hexagonal close packing of H_2TTDPz molecules due to side-by-side intermolecular S…N contacts (Fig. 1.15(a)). This planar two-dimensional layer was stacked due to π–π interactions, as in the structure of graphite. Among the three polymorphs, the three-dimensional interactions in the crystal of such an α-form seemed most appropriate to study the electrical conductivity of MTTDPz compounds. In addition, this crystal structure was strongly expected to form self-assembling films. Therefore, in this study, thin films of H_2TTDPz were fabricated, and their structures, fundamental electron transport properties and electrochemical doping were investigated.

Table 1.1. Classification of crystal structures of MTTDPz (M = H_2, Fe, Co, Ni, Cu, and Zn).

H_2	Fe	Co	Ni	Cu	Zn
α			α	α	
	β	β			β
			γ	γ	

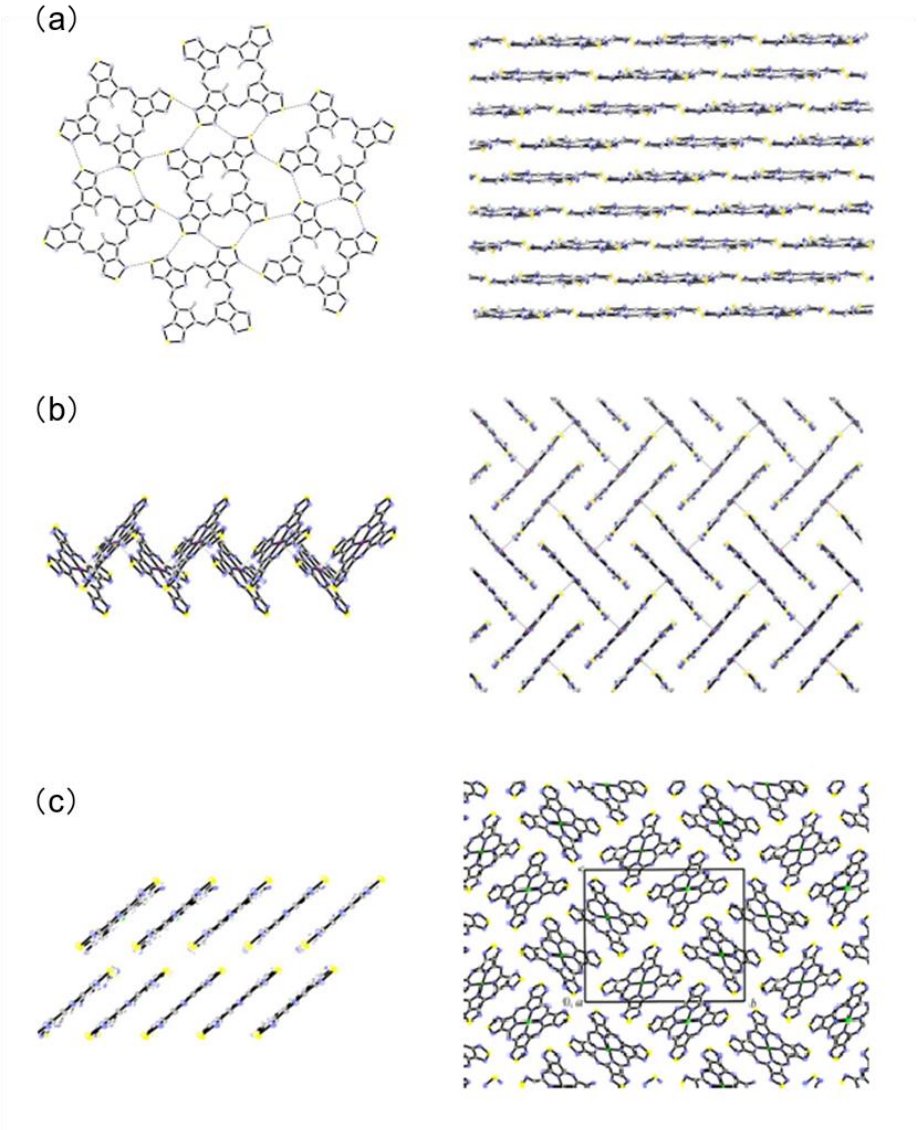

Figure 1.15. Crystal structure of MTTDPz. (a) α-form (M = H_2, Ni, and Cu), (b) β-form (M = Fe, Co, and Zn), and (c) γ-form (M = Ni and Cu), respectively.

1.3.2 Lithium Phthalocyanine

Lithium phthalocyanine (LiPc; Fig. 1.16(a)) is well known as a stable neutral radical,[65] while most phthalocyanines have a closed shell system. Since the central metal ion is a monovalent lithium cation, the corresponding −1 charge is delocalized over SOMO of Pc ligand. LiPc has been studied with respect to its intrinsic paramagnetic properties and electrical conductivity in the solid state.[66–68] The single crystal of LiPc shows a low resistivity of *ca.* 10^3 Ω cm that is superior to those of the usual Pcs with divalent central metal ions (~ 10^7 Ω cm). The crystal structure of LiPc was found to show crystalline polymorphs, resulting in three different structures, an α- and β-form with a monoclinic unit cell, and an x-form with a tetragonal unit cell (Fig. 1.16). Among them, the x-form is a unique structure, while the α and β structures are more common for unsubstituted divalent phthalocyanine compounds. The crystal structure of x-LiPc[69] is the same as that of NiPcI (Fig. 1.12).[57] In the x-form structure, the Pc molecules are stacked in a face-to-face configuration and show better overlap between neighboring molecular planes than those in the α- and β-forms.[70] A

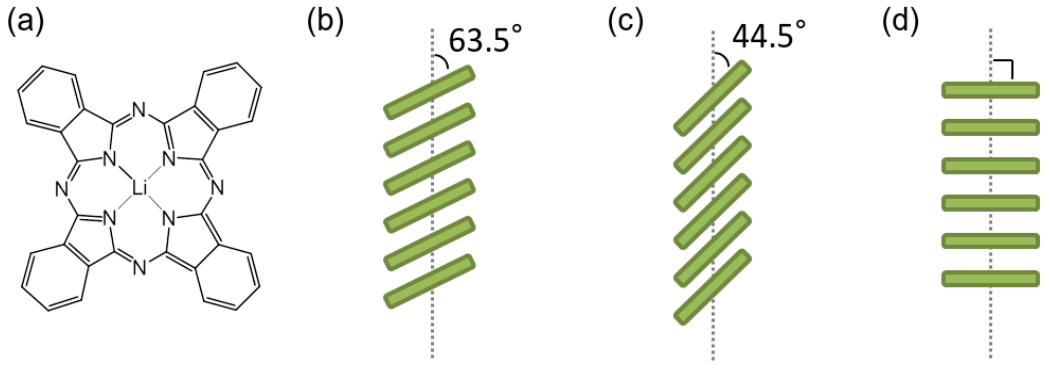

Figure 1.16. (a) Molecular structure of lithium phthalocyanine. Schematic illustration of molecular column of lithium phthalocyanines in (b) α-form, (c) β-form, and (d) *x*-form.

one-dimensional channel in the x-form is also an important feature of x-LiPc, as shown in Fig. 1.17 The size of this channel is comparable to the size of a small atom or molecule. Therefore, gas molecules such as nitrogen and oxygen can be included in the crystal through the channels. It is known that the EPR linewidth of x-LiPc becomes broad in proportion to the concentration of oxygen in the surrounding air.[69] This result indicates that the channels in the x-form are capable of modulating the physical properties of the LiPc crystal by introducing dopant ions electrochemically into the channel.

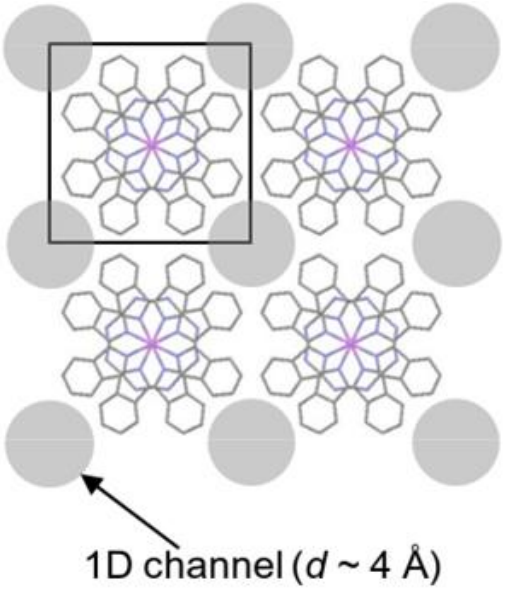

Figure 1.17. Crystal structure of x-LiPc. Gray circles represent one-dimensional channels with a diameter of *ca*. 4 Å extending along the stacking axis (*c* axis).

1.4 Motivation of This Thesis

There are a number of studies addressing the subject of band-filling control, but most of the previous works have failed to maintain the crystal structure during the filling control, with the exception of the works described in Section 1.2. The motivation of this thesis was to modulate the physical properties of organic compounds by controlling the band-filling while maintaining the band structure.

To achieve this purpose, an electrochemical doping technique was chosen for the band-filling control, namely, an electrochemical band-filling control. Electrochemical doping requires that molecules are insoluble in electrolyte solutions and a robust crystal structure is maintained during the doping as schematically illustrated in Fig. 1.18. In this work, H_2TTDPz and LiPc were chosen as appropriate molecules to satisfy these requirements. The crystal structure of H_2TTDPz exhibited short contacts through S or N atoms in addition to π–π interactions between 2D layers (see Fig. 1.15(a)). Such multi-dimensional interactions take advantage of the formation of a robust structure to the penetration of counter ions during electrochemical doping. In the case of LiPc, the x-form structure contains a one-dimensional channel along the

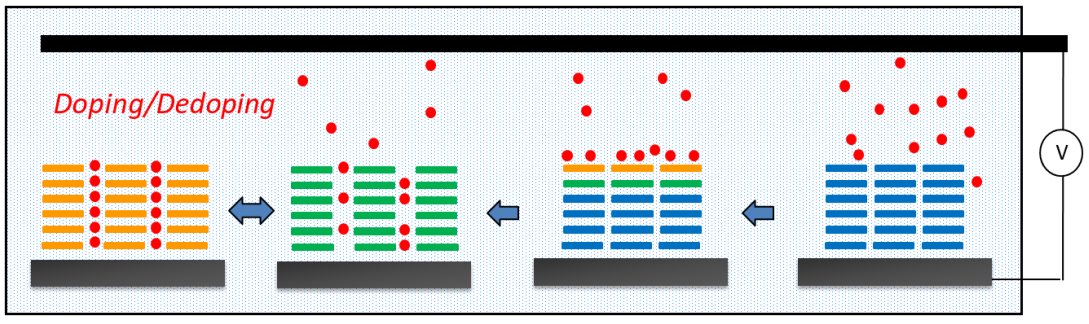

Figure 1.18. Schematic illustration of electrochemical band-filling control. Red circles represent counter ions. Blue, green, and orange rectangles represent molecules of neutral, weakly-doped, and highly-doped state, respectively.

stacking axis of Pcs. When the crystal of x-LiPc is electrochemically oxidized or reduced, it is expected that counter ions will occupy vacant spaces within the channels without significant structural changes, since the channel size seems to be large enough to accommodate counter ions.

In Chapter 2, thin films of H_2TTDPz were fabricated on ITO substrates and their fundamental physical properties, such as electrochemistry and electron transports, were evaluated, and then electrochemical doping of H_2TTDPz was examined. In Chapter 3, electrochemical doping of LiPc thin films was carried out, and the robustness of the thin film structure and electrical resistivity with relation to its structural features were discussed. In Chapter 4, electrochemical doping of single crystalline x-LiPc was performed to discuss the band-filling in greater detail, since the structural defects of thin films are undesirable for interpreting the relationship between crystal structures and intrinsic physical properties. A summary of the thesis is given in Chapter 5.

References

1. H. Akamatu, H. Inokuchi, Y. Matsunaga, *Nature* **1954**, *173*, 168–169.
2. J. M. Williams, A. J. Schultz, U. Geiser, K. D. Carlson, A. M. Kini, H. H. Wang, W. Kwok, M. Whangbo, J. E. Schirber, *Science*, **1991**, *252*, 1501–1508.
3. D. S. Acker, R. J. Harder, W. R. Hertler, W. Mahler, L. R. Melby, R. E. Benson, W. E. Mochel, *J. Am. Chem. Soc*. **1960**, *82*, 6408–6409.
4. D. L. Coffen, *Tetrahedron Lett*. **1970**, *11*, 2633–2636.
5. F. Wudl, G. M. Smith, E. J. Hufnagel, *J. Chem. Soc., Chem. Commun*. **1970**, 1453.
6. J. P. Ferraris, D. O. Cowan, V. Walatka, Jr., J. H. Perlstein, *J. Am. Chem. Soc*.**1973**, *95*, 948–949.
7. L. B. Coleman, M. J. Cohen, D. J. Sandman, F. G. Yamagishi, A. F. Garito, A. J.

Heeger, *Solid State Commun*. **1973**, *12*, 1125–1132.

8. D. Jerome, A. Mazaud, M. Rebaulet, K. Bechgaard, *J. Phys. Lett. (Paris)* **1980**, *41*, L-95.
9. A. J. Banister, N. Bricklebank, I. Lavender, J. M. Rawson, C. I. Gregory, B. K. Tanner, W. Clegg, M. R. J. Elsegood, F. Palacio, *Angew. Chem. Int. Ed*. **1996**, *35*, 2533–2535.
10. N. F. *Mott,Metal-Insulator Transitions*, 2nd ed., Taylor and Francis, London, **1990**.
11. A. J. Epstein, S. Etemad, A. F. Garito, A. J. Heeger, *Phys. Rev. B* **1972**, *5*, 952–977.
12. A. F. Garito, A. J. Heeger, *Acc. Chem. Res*. **1974**, *7*, 232–240.
13. G. Saito, T. Enoki, K. Toriumi, H. Inokuchi, *Solid State Commun*.**1982**, *42*, 557–560.
14. K. Kanoda, *Hyperfine Interactions*, **1997**, *104*, 235–249.
15. K. Kanoda, *Physica C*, **1997**, *282–287*, 299–302.
16. J. S. Miller, A. J. Epstein, *Angew. Chem. Int. Ed*. **1987**, *26* 287–293.
17. J. S. Miller, A. J. Epstein, *Solid State Communications* **1987**, *27*, 325–329.
18. F. Wudl, D. Wobschall, E. J. Hufnagel, *J. Am. Chem. Soc*. **1972**. *94*. 670–672.
19. SJ. La Placa, P. W. R. Corfield, R. Thomas, B. A. Scott, *Solid State Communications* **1975**, *17*, 635–638
20. R. B. Somoano, A. Gupta, V. Hadek, T. Datta, M. Jones, R. Deck, A. M. Hermann, *J. Chem. Phys*. **1975**, *63*, 4970–4976.
21. J. B. Torrance, B. A. Scott, B. Welber, F. B. Kaufman, P. E. Seiden, *Physical Review B* **1979**, *19*, 730–741.
22. T. Sugano, K. Yakushi, H. Kuroda, *Bull. Chem. Soc. Jpn*. **1978**, *51*, 1041–1046.
23. T. Hasegawa, K. Inukai, S. Kagoshima, T. Sugawara, T. Mochida, S. Sugiura, Y.

Iwasa, *Synth. Met*. **1997**, *86*, 1801–1802.

24. T. Hasegawa, K. Inukai, S. Kagoshima, T. Sugawara, T. Mochida, S. Sugiura, Y. Iwasa, Chem. Commun. **1997**, *18*, 1377–1378.
25. M. J. Rossinsky, D. W. Murphy, R. M. Fleming, R. Tycko, A. P. Ramirez, T. Siegrist, G. Dabbagh, S. E. Barrett, *Nature* **1992**, *365*, 416–418.
26. A. F. Hebard, M. J. Rosseinsky, R. C. Haddon, D. W. Murphy, S. H. Glarum, T. T. M. Palstra, A. P. Ramirez, A. R. Kortan, *Nature* **1991**, *350*, 600–601.
27. P. W. Stephens, L. Mihaly, P. L. Lee, R. L. Whetten, S. Huang, R. Kaner, F. Deiderich, K. Holczer, *Nature* **1991**, *351*, 632–634.
28. P. W. Stephens, L. Mihaly, J. B. Wiley, S. Huang, R. B. Kaner, F. Diederich, R. L. Whetten, K. Holczer, *Phys. Rev. B* **1992**, *45*, 543–546.
29. T. Yildirim, L. Barbedette, J. E. Fischer, C. L. Lin, J. Robert, P. Petit, T. T. M. Palstra, *Phys. Rev. Lett*. **1996**, *77*, 167–170.
30. K. Tanigaki, T. W. Ebbesen, S. Saito, J. Mizuki, J. S. Tsai, Y. Kubo, S. Kuroshima, *Nature* **1991**, *352*, 222–223
31. T. Yildirim, J. E. Fischer, R. Dinnebier, P. W. Stephens, C. L. Lin, *Solid State Commun*. **1995**, *93*, 269–274.
32. M. J. Panzer, C. D. Frisbie, *Adv. Func. Mat*. **2006**, *16*, 1051–1056.
33. M. J. Panzer, C. R. Newman, C. D. Frisbie, *Appl. Phys. Lett*. **2005**, *86*, 103503.
34. J. Lee, M. J. Panzer, Y. He, T. P. Lodge, C. D. Frisbie, *J. Am. Chem. Soc*. **2007**, *129*, 4532–4533.
35. M. J. Panzer, C. D. Frisbie, *J. Am. Chem. Soc*. **2007**, *129*, 6599–6670.
36. M. J. Panzer, C. D. Frisbie, *Adv. Mater*. **2008**, *20*, 3177–3180.
37. H. Shimotani, G. Diguet, Y. Iwasa, *Appl. Phys. Lett.* **2005**, *86*, 022104

38. K. Ueno, S. Nakamura, H. Shimotani, A. Ohtomo, N. Kimura, T. Nojima, H. Aoki, Y. Iwasa, *Nature Mater*. **2008**, *7*, 855–858.

39. P. J. Nigrey, A. G. MacDiarmid, A. J. Heeger, *J. Chem. Soc., Chem. Commun.* **1979**, 594–595.

40. G. Tourillon, F. Garnier, *J. Electroanal. Chem*. **1984**, *161* 407–414.

41. P. M. McManus, S. C. Yang, R. J. Cushman, *J. Chem. Soc., Chem. Commun.* **1985**, 1556–1557.

42. T. Tominaga, K. Hayashi, N. Toshima, *J. Porphyrins Phthalocyanines*, **1997**, *1*, 239–249.

43. T. Maruno, S. Hayashida, K. Sukegawa, *J. Electroanal. Chem*. **1989**, *267*, 303–307.

44. J. M. Green, L. R. Faulkner, *J. Am. Chem. Soc.* **1983**, *105*, 2950–2955.

45. Y. Takigawa, R. Watanabe, S. Morita, Y. F. Miura, M. Sugi, *Jpn. J. Appl. Phys*, **2006**, *45*, 394–396.

46. W. Koh, D. Dubois, W. Kutner, M. T. Jones, K. M. Kadish, *J. Phys. Chem*. **1993**, *97*, 6871–6879.

47. J. G. Gaudiello, M. Almeida, T. J. Marks, W. J. McCarthy, J. C. Butler, C. R. Kannewurf, *J. Phys. Chem*. **1986**, *90*, 4917–4920.

48. J. G. Gaudiello, G. E. Kellogg, S. M. Tetrick, T. J. Marks, *J. Am. Chem. Soc.* **1989**, *111*, 5259–5271.

49. M. Almeida, J. G. Gaudiello, G. E. Kellogg, S. M. Tetrick, H. O. Marcy, W. J. McCarthy, J. C. Butler, C. R. Kannewurf, T. J. Marks, *J. Am. Chem. Soc.* **1989**, *111*, 5271–5284.

50. C. C. Leznoff, A. B. P. Lever, *Phthalocyanines: Properties and Applications, Vol. 4*, VCH Publications, New York, **1996**.

51. P. Peumans, S. Uchida, S. R. Forrest, *Nature*, **2003**, *425*, 158–162.
52. Z. Bao, A. J. Lovinger, A. Dodabalapur, *Appl. Phys. Lett*. **1996**, *69*, 3066–3068.
53. J. Blochwitz, M. Pfeiffer, T. Fritz, K. Leo, *Appl. Phys. Lett*. **1998**, *73*, 729–731.
54. M. Hanack, M. Lang, *Adv. Mater.* **1994**, *6*, 819–833.
55. J. L. Petersen, C. S. Schramm, D. R. Stojakovic, B. M. Hoffman, T. J Marks, *J. Am. Chem. Soc*. **1977**, *99*, 286–288.
56. C. J. Schramm, D. R. Stojakovic, B. M. Hoffman, T. J. Marks, *Science*, **1978**, *200*, 47–48.
57. C. J. Schramm, R. P. Scaringe, D. R. Stojakovic, B. M. Hoffman, J. A. Ibers, T. J. Marks, *J. Am. Chem. Soc*. **1980**, *102*, 6702–6713.
58. T. Inabe, K. Morimoto, *Synth. Met*. **1997**, *86*, 1779–1800.
59. H. Hasegawa,T. Naito,T. Inabe, T. Akutagaw, T. Nakamura, *J. Mater. Chem*. **1998**, *8*, 1567–1570.
60. H. Inokuchi, K. Imaeda, T. Enoki, T. Mori, Y. Maruyama, G. Saito, N. Okada, H. Yamochi, K. Seki, Y. Higuchi, N. Yasuoka, *Nature* **1987**, *329*, 39–40.
61. P. A. Stuzhin, E. M. Bauer, C. Ercolani, *Inorg. Chem*. **1998**, *37*, 1533–1539.
62. E. M. Bauer, D. Cardarrilli, C. Ercolani, P. A. Stuzhin, U. Russo, *Inorg. Chem*. **1999**, *38*, 6114–6120.
63. M. Fujimori, Y. Suzuki, H. Yoshikawa, K. Awaga, *Angew. Chem. Int. Ed*. **2003**, *42*, 5863–5865.
64. Y. Suzuki, M. Fujimori, H. Yoshikawa, K. Awaga, *Chem. Eur. J*. **2004**, *10*, 5158–5164.
65. H. Sugimoto, T. Higashi, M. Mori, *J. Chem. Soc., Chem. Commun*. **1983**, 622–623.
66. P. Turek, J.-J. Andre, A. Giraudeau, *Chem. Phys. Lett*. **1987**, *134*, 471–476.

67. P. Turek, M. Moussavi, P. Petit, J.-J. Andre, *Synth. Met.* **1989**, *29*, F65–F70.

68. F. Bensebaa, J.-J. Andre, *J. Phys. Chem*. **1992**, *96*, 5739–5745.

69. H. Sugimoto, M. Mori, H. Masuda, T. Taga, *J. Chem. Soc., Chem. Commun*. **1986**, 962–963.

70. M. Brinkmann, P. Turek, J.-J. Andre, *J. Mater. Chem*. **1998**, *8*, 675–685.

Chapter 2. Electrochemical Doping of Tetrakis(thiadiazole)porphyrazine Thin Films

2.1 Introduction

As discussed in Section 1.2.4, the electrochemical doping is a useful method with various advantages such as precise control of doping degree and reproducibility, which are obtained by the electrode potential tuning. Since this process is associated with penetrations of counter cations or anions into the molecular assembly, thin film is a favorite sample form rather than crystalline samples. Despite such important advantages, electrochemical doping has not been a popular method especially for molecular materials, since small molecules are highly soluble to common organic or aqueous electrolyte solutions. In addition, the other crucial disadvantage for applying this technique to molecular solids is that counter cations or anions penetrating into the molecular assembly to maintain a charge balance can cause a collapse of the crystal structures. To avoid these difficulties of the electrochemical doping, we need structurally-robust organic thin films, which are formed by a strong π–π interactions, electrostatic interactions, coordination bonding, etc. In this perspective, tetrakis(thiadiazole)porphyrazine series MTTDPz are quite promising (see Section 1.3.1). The crystal structures of the first transition metal compounds can be classified into three forms, α, β, and γ, in which MTTDPz always exhibit a 3D network structure caused by π–π interactions, $S^{\delta+}\cdots N^{\delta-}$ electrostatic interactions, M…N intermolecular coordination bondings.[1,2] Particularly, the crystal form α, which are found in the

metal-free, copper and nickel derivatives, consists of a two-dimensional hexagonal close packing of MTTDPz molecules due to side-by-side intermolecular S…N contacts, which are stacked due to π–π interactions, like a molecular graphite. This α-form seemed most appropriate for thin film fabrication and electrochemical band filling control.

In Chapter 2, we firstly describe the synthesis of H_2TTDPz, and its thin-film fabrication and characterization. Then we show the performance of thin-film photocells and field effect transistor of H_2TTDPz, providing firm evidences that this material operates as an *n*-type semiconductor in contrast that most of the phthalocyanine analogues are *p*-type semiconductors. Lastly we discuss the electrochemistry and electrochemical doping of H_2TTDPz thin films.

2.2 Synthesis

H_2TTDPz was synthesized according to the previously reported procedure[3] with a minor modification (Scheme 2.1).

2.2.1 3,4-dicyano-1,2,5-thiadiazole (DCTD)

A mixture of diaminomaleonitrile (10.8 g, 0.1 mol) and $SOCl_2$ (35.7 g, 0.3 mol) was first heated at 60°C for about 30 minutes until a mixture became a homogeneous liquid and then refluxed for 2 hours. Excess $SOCl_2$ was evaporated under reduced pressure. The solid was dissolved in 400 mL of diethyl ether. The ether solution was washed with water, and then dried over sodium sulfate. After evaporating the ether under reduced pressure, the crude product was obtained and dried in ambient air.

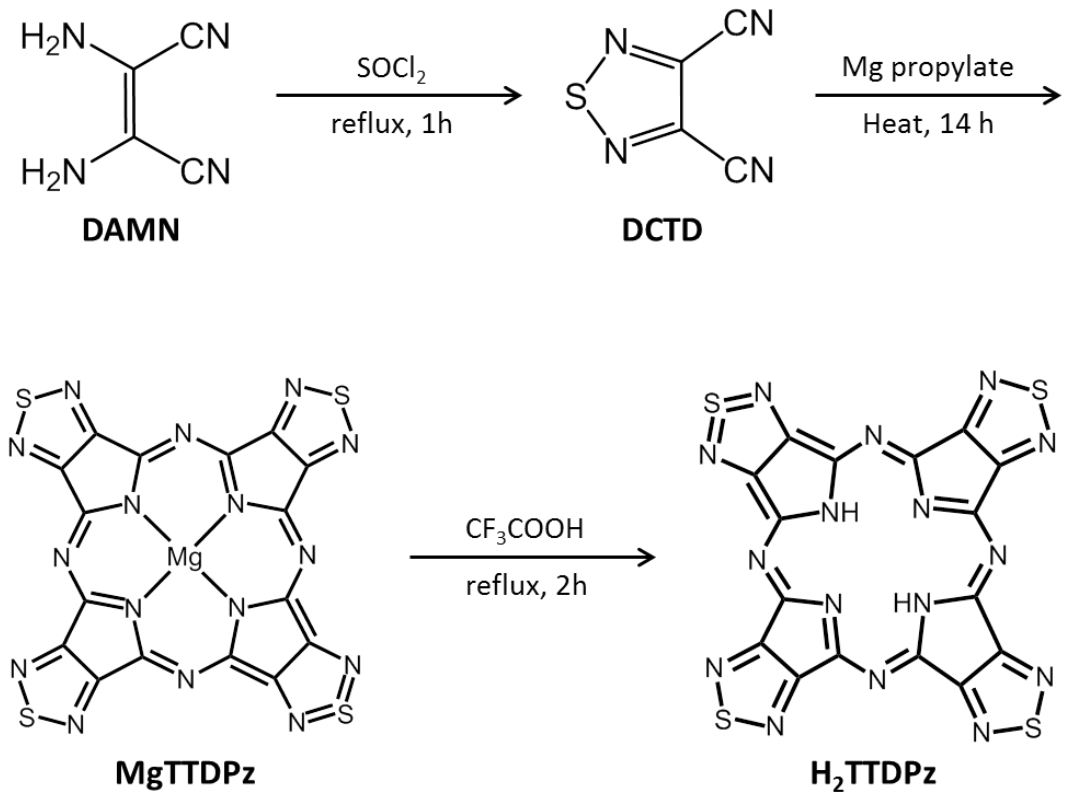

Scheme 2.1 Synthetic scheme of H_2TTDPz.

2.2.2 [TTDPzMg(H_2O)]·CH_3COOH

Magnesium turnings (0.75 g, 0.031 mol) were suspended in 30 mL of 1-propanol in a dry flask under nitrogen atmosphere, and a small amount of I_2 was added to the flask. The suspension was refluxed for 8 hours to complete a conversion of Mg into its corresponding propylate. After cooling the reaction mixture, DCTD (4.22 g, 30 mmol) was added to the suspension, and the mixture was refluxed again at 120°C for 14 hours. During the reaction, the gray mixture became green and then dark blue. Propanol was eliminated by evaporation under reduced pressure, and 400 mL of CH_2Cl_2 was added to the solid blue material to dissolve unreacted DCTD. After filtration, the solid material was suspended in 200 mL of 50% acetic acid and stirred at room

temperature for 1 hour. After filtration, the solid material was washed repeatedly with water to neutral pH, and then dried under vacuum (1.58 g; yield 47%).

2.2.3 H_2TTDPz

The solvated MgTTDPz (1.0 g, 1.55mmol) was suspended in CF_3COOH (10 mL), and the mixture was refluxed for 2 hours. After cooling, 15 mL of H_2O was added and the mixture was heated again for 20 min. After filtration, the dark blue material was washed with water to neutral pH and dried under vacuum (0.34 g, 0.5 mmol; yield 35%).

2.2.4 Purification of H_2TTDPz

H_2TTDPz was purified by sublimation method. 100 mg of crude H_2TTDPz was put in a quartz boat, and the sample boat was placed in a quartz tube (100 mm in diameter). The sample was heated at 430°C for 12 hours under reduced pressure with a stream of nitrogen gas as a carrier from one end of the quartz tube at a rate of 50 mL/min. Pure H_2TTDPz was obtained as purple microcrystals (10–30 mg). Elemental analysis (%): Calc. C, 35.16; H, 0.37; N, 41.00. Found: C, 35.41; H, 0.16; N, 41.61.

2.3 Fabrication and Characterization of Thin Films

H_2TTDPz thin films of 100 nm in thickness were prepared by vacuum vapor deposition. 15 mg of H_2TTDPz (purified by sublimation prior to use) was put in an alumina crucible. The temperature of sample crucible was controlled by resistive heating of surrounded tungsten wires. The pressure in the deposition chamber was less than 5×10^{-4} Pa before the deposition and was *ca*. 1×10^{-3} Pa during the deposition. A deposition rate was monitored by a quartz crystal microbalance placed adjacent to substrates and kept at a rate of 1.2–1.8 nm/min during the deposition by tuning the temperature of crucible. Fig. 2.1 shows an AFM image of a thin film on Si(100). The image indicates good overlaps between the grains and a very flat surface; the height difference between the top and bottom on this surface is less than 20 nm. Fig. 2.2 shows the XRD patterns of the thin films on ITO substrate. They commonly include a peak at 2θ = 27.3°, which corresponds to an interlayer distance of 0.33 nm. Since this value is

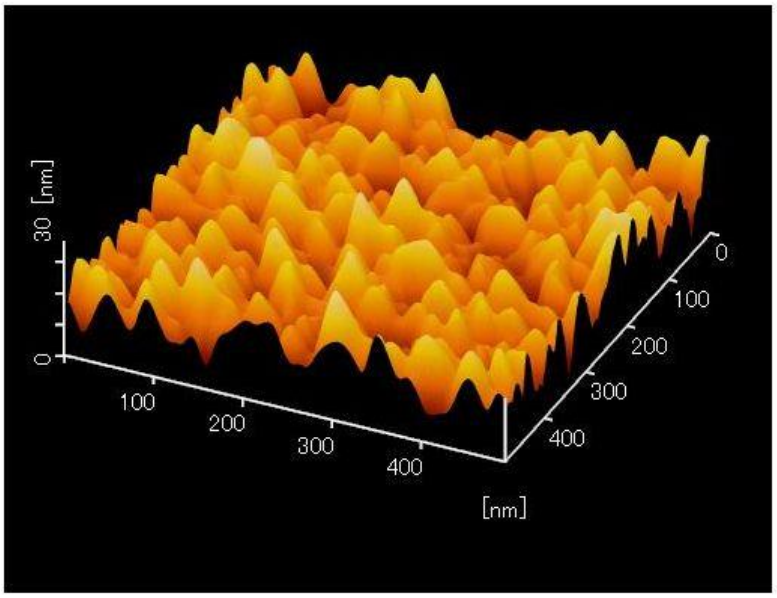

Figure 2.1 AFM image of H_2TTDPz thin film on Si(100).

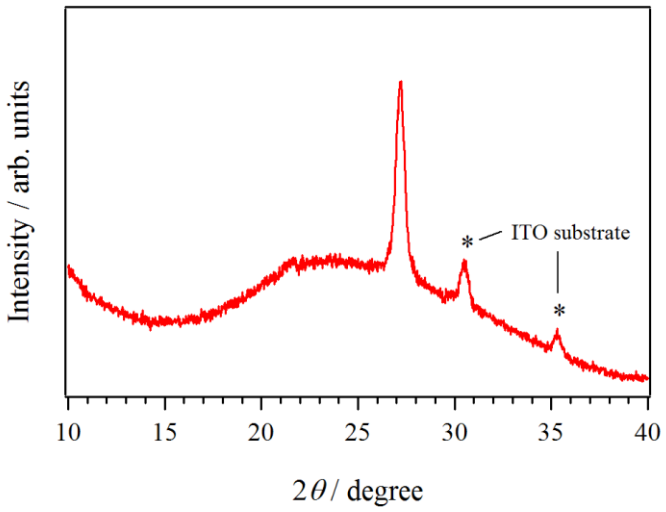

Figure 2.2 XRD patterns of H_2TTDPz thin films ITO substrate.

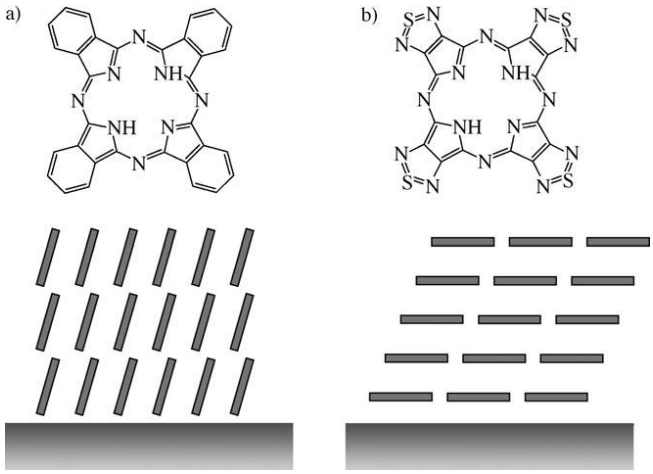

Figure 2.3 Molecular arrangements of H_2Pc (a) and H_2TTDPz (b) on the substrate.

nearly the same as that in the bulk crystal (0.345 nm), it is reasonable to conclude that the thin films of H_2TTDPz consist of a lamellar structure in which the molecular planes are all parallel to the surfaces of the substrate, as shown in Fig 2.3. It is known that H_2Pc thin films show a strong peak at 2θ = 6.7° in the XRD pattern,[4] indicating that the

molecules are aligned in crystal grains with molecular plane nearly perpendicular to the substrate surface, as illustrated in Fig 2.3. This type of perpendicular molecular plane alignment is typical for the thin films of organic π molecules, because this type of structure is advantageous for gaining both π–π stacking stabilization and a high density on a unit area of the substrates. In other words, the structure of H_2TTDPz thin films, namely, parallel molecular plane alignment with respect to the substrate surface, is very unusual and is indicative of the strong propensity of H_2TTDPz to self-assemble into a 2D sheet structure.

2.4 Photoconductivity of H_2TTDPz Thin Films

Thiadiazole rings possess electron-withdrawing properties due to their electronegativity and thus H_2TTDPz indicates a good electron-acceptability and has potential of *n*-type behavior in the electronic devices. Energy levels of H_2TTDPz were investigated in the real device of sandwich cell of ITO/H_2TTDPz/metal architecture by means of the photocurrent-action spectra to discuss its *n*-type character.

2.4.1 Device Fabrication

H_2TTDPz sandwich cells were adopted for the photocurrent measurements (Fig. 2.4), and fabricated them as follows.[5] First, a thin film of H_2TTDPz was evaporated onto a glass substrate on which a 2 mm-width ITO electrode of thickness 100 nm was formed. Then a 2 mm-width Au or Al electrode with a thickness of 50 nm was evaporated onto the film perpendicular to the ITO electrode. The effective sample area was 0.04 cm^2. In order to avoid short circuiting, the thickness of H_2TTDPz was set to 200 nm, which was longer than the light penetration depth of 80 nm at the top of the

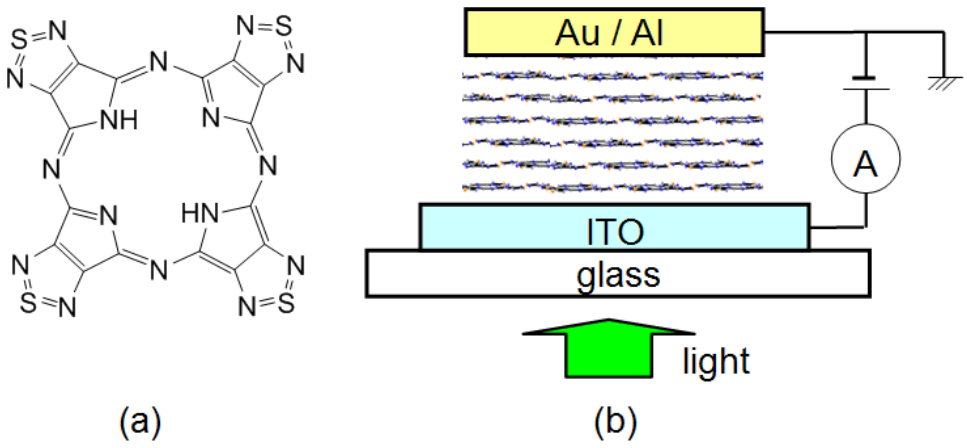

Figure 2.4 (a) Molecular structure of H_2TTDPz, (b) Schematic view of photocurrent measurement system.

Q-band.

The dc and ac photocurrent measurements were carried out with a 500-W halogen lamp.[5] The light intensity was calibrated with a Si photodiode. The monochromated light was allowed to illuminate the transparent ITO electrode, and the photocurrent was recorded under vacuum. To obtain the photocurrent action spectra, the light was chopped with a frequency of 17–18 Hz, and the signals were detected by a two-phase lock-in amplifier.[5] The ac voltage appearing on a series resistance (1 MΩ) was measured under applied dc bias between two electrodes. The photocurrent-action spectra were then normalized in such a way that the incident photon number was constant (10^{15}/cm^2).

2.4.2 Photoconductivity

Fig. 2.5 shows the *I-V* characteristics of an (+)ITO/H_2TTDPz (200 nm)/Au(–) cell, shown in Fig. 2.4. In the dark state, a clear rectifying behavior was observed (black

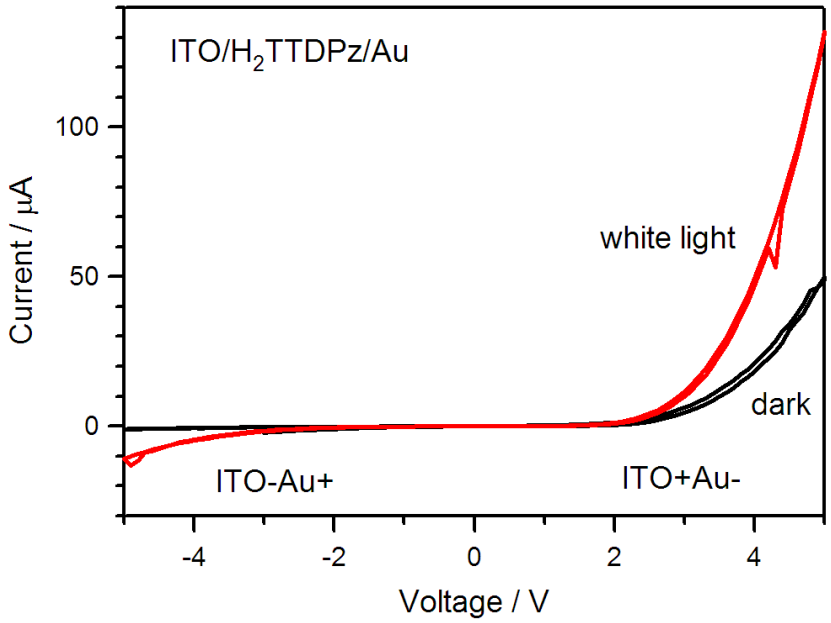

Figure 2.5. *I-V* characteristics of an (+)ITO/H_2TTDPz (200 nm)/Au(–) cell.

curve), indicating the presence of a Schottky barrier, while, under illumination of white light, photocurrent was observed for both bias directions (red curve). The photocurrent quantum yield was calculated as approximately 0.1 % under light illumination of 532 nm. Fig. 2.6 shows the photocurrent action spectra with bias voltages of –2 (pink), –1 (orange), 1 (green), and 2 V (blue), applied to the ITO electrode. This figure also shows the optical absorption spectrum of a 100-nm film of H_2TTDPz as a broken curve. When the ITO was negatively biased (pink and orange), the photocurrent appeared in the range of photon energy above 1.4 eV, with a maximum of 1.8 eV. After passing through a minimum at 2.5 eV, the photocurrent increased again. These action spectra are nearly in phase with the optical absorption, representing 'symbatic' behavior. When the ITO was positively biased (green and blue curves), however, the action spectra reached three maximums at 1.6, 2.2, and 2.8 eV, being out of phase with the photoabsorption ('antibatic' behavior).

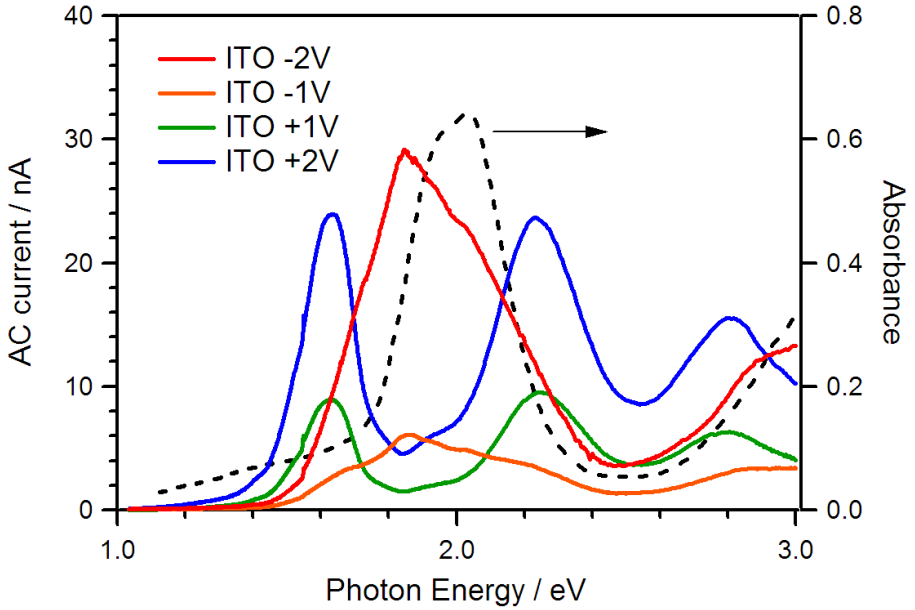

Figure 2.6 Photocurrent action spectra with bias voltages of –2 (pink), –1 (orange), 1 (green), and 2 V (blue), applied to the ITO electrode.

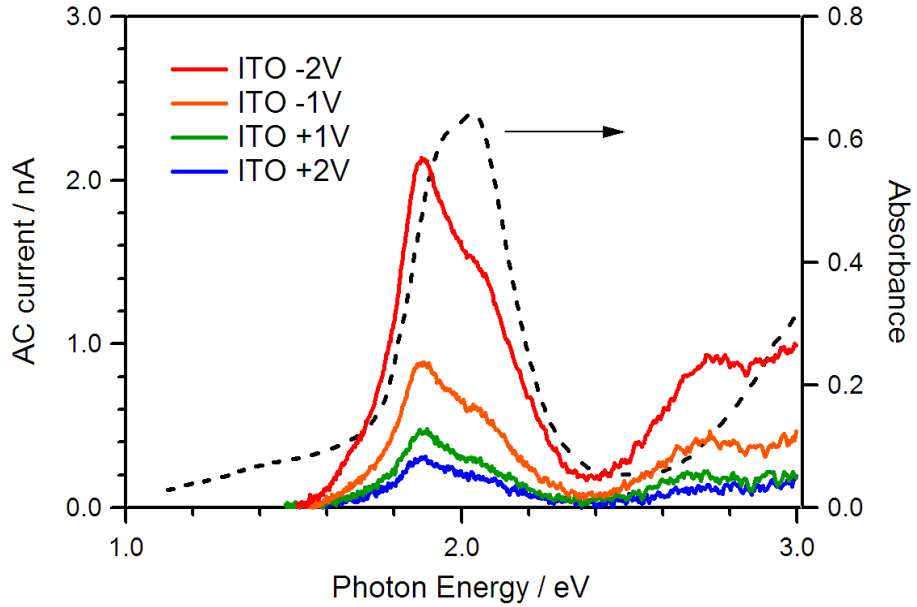

Figure 2.7 Photocurrent action spectra of an (+)ITO/H_2TTDPz (200 nm)/Al(–) photocell under biases of –2 (pink), –1 (orange), 1 (green), and 2 V (blue).

Fig. 2.7 shows the photocurrent action spectra of an (+)ITO/H_2TTDPz (200 nm)/Al(–) photocell under biases of –2 (pink), –1 (orange), 1 (green), and 2 V (blue). When the Au anode was replaced with Al, the photocurrent became much smaller. In addition, the photocurrent always exhibited symbatic behavior under biases between 2 and –2 V.

The observed symbatic and antibatic behavior and the significant dependence on the anode metal can be explained as follows. Schottky-type photocells are known to exhibit a so-called filter effect in photocurrent action spectra, in case in which the film thickness is larger than the light penetration depth.[5–7] More specifically, it is the light absorption near the Schottky contact that results in effective dissociation of excitons into free carriers because the electric field is concentrated on the barrier region.[7] The excitons far from the blocking contact cannot reach the barrier region, so they would recombine geminately without producing photocarriers.

Since the major carrier in *n*-type semiconductors is electrons, their photocurrent should be dominated by photocarriers generated near the negatively biased electrode, forming a blocking or Schottky contact with the *n*-type materials.[8–11] After charge separation near the negative electrode, the positive carriers or holes are easily absorbed into this electrode and electrons as negative carriers travel to the opposite positive electrode, producing photocurrent. Therefore, when the negative electrode is illuminated, the photocarrier yield is proportional to the light intensity and the photocurrent action spectrum coincides with the optical absorption spectrum of the semiconductor, resulting in ‘symbatic’ behavior. If the positive electrode is illuminated, however, the light intensity might attenuate before reaching the negative electrode at which the photocarriers are generated, due to a strong absorption in the organic

semiconductors. Therefore, a larger photocurrent is expected at the absorption edges than at the absorption center, because such weakly absorbed light can reach the negative electrode and can induce charge separation there. The photocurrent action spectrum becomes out of phase with the optical absorption spectrum, resulting in 'antibatic' behavior.

Fig. 2.8 schematically shows the work functions of the ITO and Au electrodes as well as the HOMO and LUMO levels of H_2TTDPz. The expected charge separation region in the ITO/H_2TTDPz/Au photocell is indicated as a yellow oval. Photoelectron

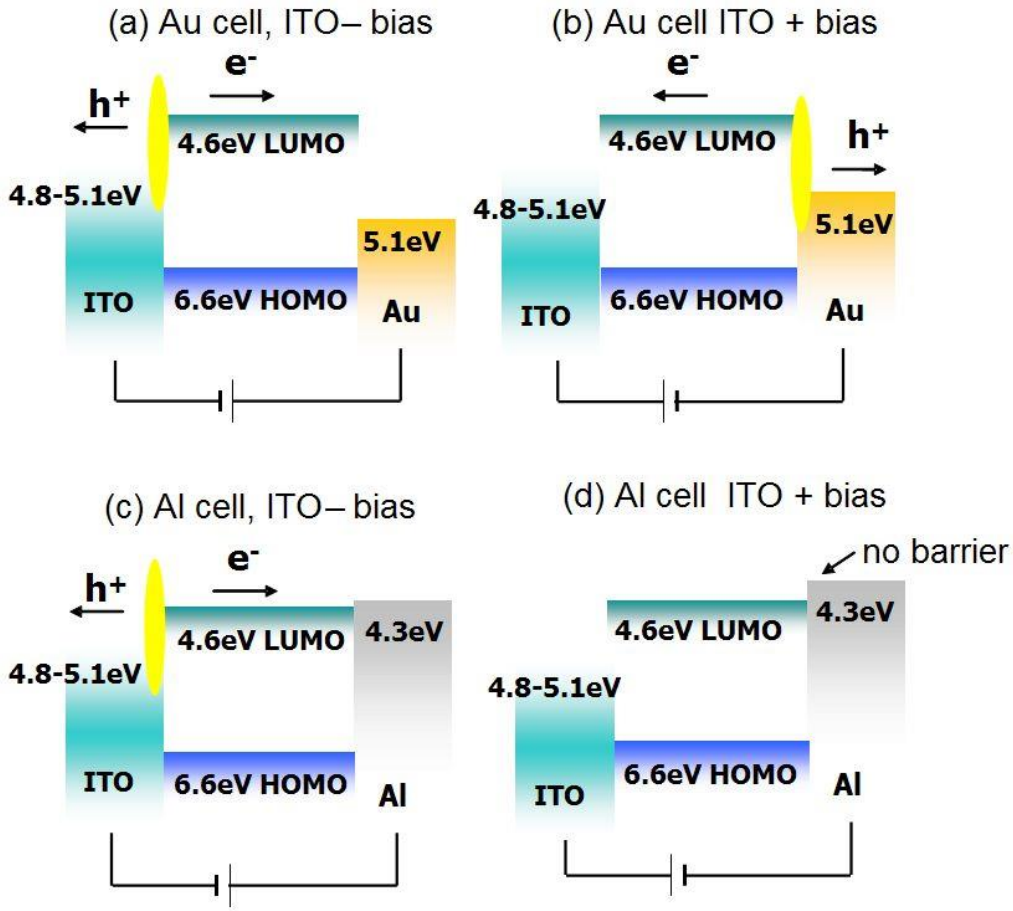

Figure 2.8 Schematic view of energy levels of the ITO and Au electrodes, and the HOMO and LUMO levels of H_2TTDPz for various photocells.

spectroscopy and photoabsorption spectroscopy on H_2TTDPz suggest that the LUMO and HOMO levels of H_2TTDPz are 4.6 and 6.6 eV, respectively, from the vacuum level.[12] Because these levels are far from the workfunctions of ITO (4.8–5.1 eV) and Au (5.1 eV), either ITO/ H_2TTDPz or Au/H_2TTDPz contact would act as a blocking contact with a Schottky-type barrier when negatively biased. In contrast, the workfunction of Al (4.2 eV) is close to the LUMO level so that the Al contact probably forms an ohmic contact with H_2TTDPz. The symbatic and antibatic behavior and the strong electrode dependence of the ITO/H_2TTDPz/Au and ITO/H_2TTDPz/Al photocells are consistent with H_2TTDPz acting as an *n*-type semiconductor.

2.5 FET performance of H_2TTDPz Thin Films

Electrical transport property of H_2TTDPz was investigated with the actual OFET devices. Thin-film FETs of H_2TTDPz were fabricated with DEME-TFSI, as a gate electrolyte (Fig. 2.9). By using such an ionic liquid, high-density carrier

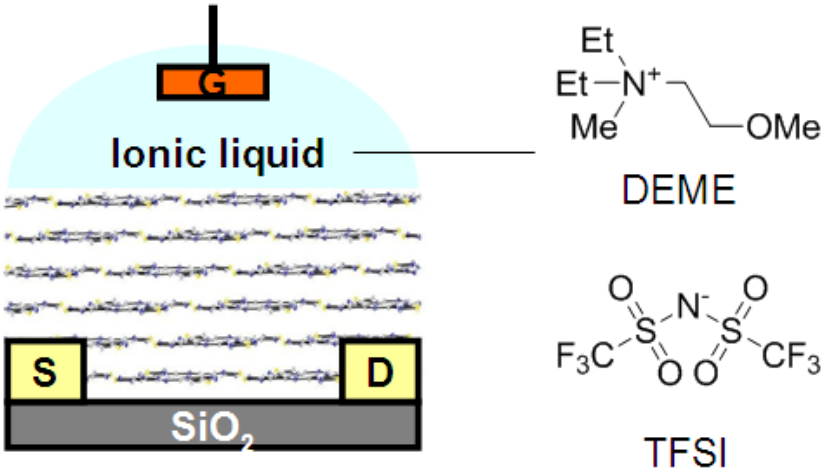

Figure 2.9 Thin-film FETs of H_2TTDPz using DEME-TFSI as a gate electrolyte.

accumulations were expected through an electric double layer (EDLs) formed on the H_2TTDPz surface in the gate electrolyte solution.

2.5.1 Fabrication of FET Devices

The FET performance of the H_2TTDPz thin films was examined using two kinds of gate materials, an ionic liquid, DEME-TFSI, and SiO_2. Thin films of H_2TTDPz with a thickness of 100 nm were prepared on interdigitated array electrodes (Pt), in which the channel dimensions correspond to W = 20 cm width and L = 10 μm length by vacuum vapor-deposition. The ionic-liquid gate was prepared by putting a droplet of a commercial ionic liquid, N,N-diethyl-N-methyl(2-methoxyethyl)ammonium bis(trifluoromethylsulfonyl)imide (abbreviated as DEME-TFSI) on the H_2TTDPz surface and inserting a Pt wire in it (Fig. 2.9). SiO_2-gate FETs of H_2TTDPz were fabricated by making its thin films (100 nm) on Au interdigitated electrode arrays prepared on the 300-nm SiO_2/doped Si substrate. The source-drain electrodes consisted of a total channel width of 20 cm and a channel length of 10 μm. The performance of these FETs was examined under vacuum.

2.5.2 FET Performance

Fig. 2.10 shows the output characteristic, namely the source-drain current I_D vs. voltage V_D plots, measured in the dark under vacuum with the gate voltages V_G = 0.0, 0.2, 0.4 and 0.6 V. There is little deviation from zero current with an increase in V_G, indicating that current leakage through the dielectric is negligibly small. Fig. 2.11 shows the transfer characteristic, namely the source-drain current $I_D^{1/2}$ vs. gate voltage V_G plots, measured in the dark under vacuum with a source-drain voltage of V_D = 0.5 V. The I_D

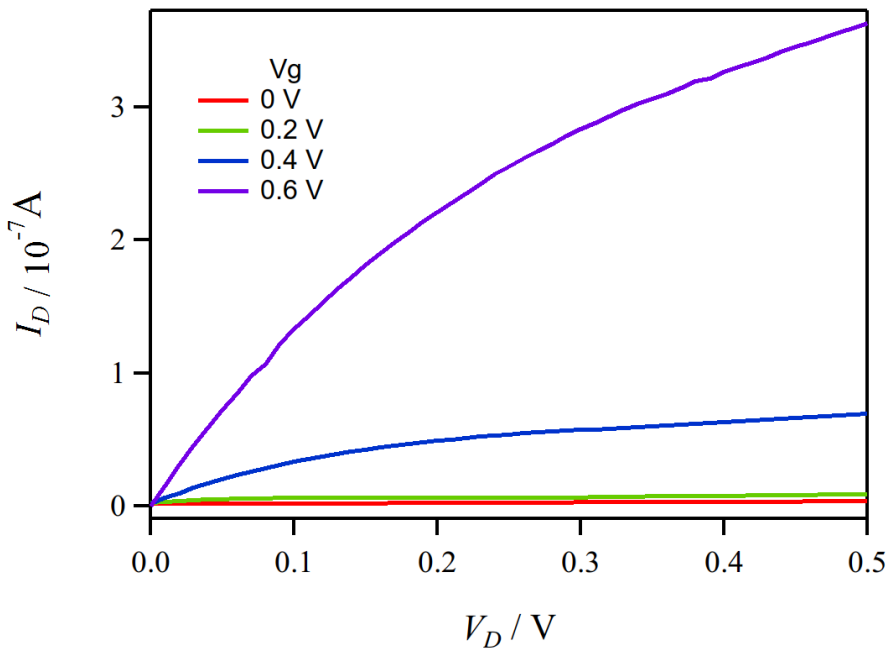

Figure 2.10 Source-drain current I_D vs. voltage V_D plots, measured in the dark under vacuum with the gate voltages V_G = 0.0, 0.2, 0.4 and 0.6 V.

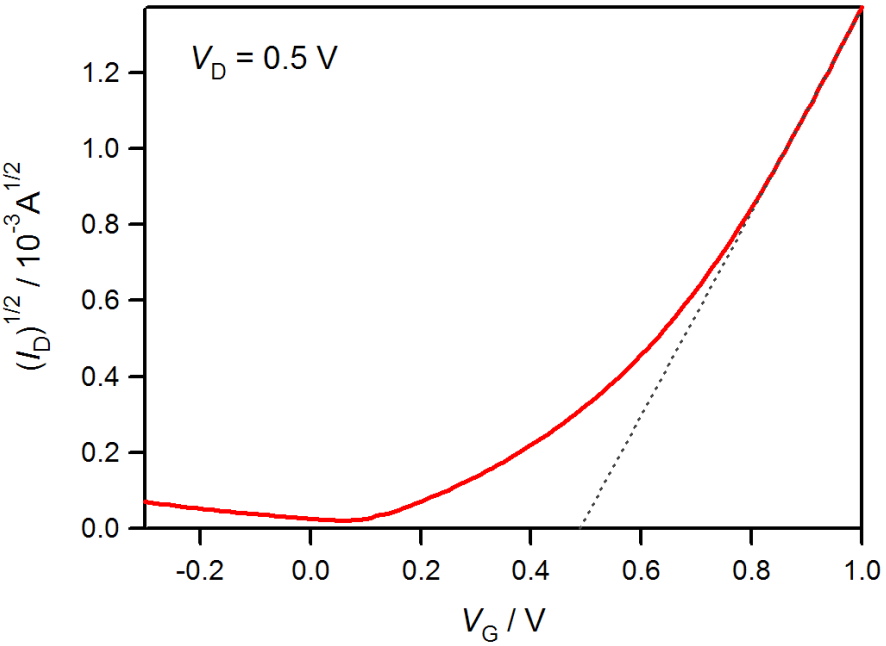

Figure 2.11 Source-drain current $I_D^{1/2}$ vs. gate voltage V_G plots, measured in the dark under vacuum with a source-drain voltage of V_D = 0.5 V.

value at V_G = 0 V is less than 1 pA, indicating that the present transistors are in normallyoff states. With an increase in V_G towards a positive value, I_D shows a quick increase above V_G = 0.2 V with an on/off ratio of *ca*. 10^4. The I_D vs. V_G curves showed a good reversibility, so that there should be no penetration of the counter cations.

This FET behavior clearly indicates that H_2TTDPz operates as an *n*-type semiconductor. The extrapolation of the $I_D^{1/2}$ vs. V_G curve from the large V_G range indicates a very low threshold voltage of V_{Gth} = 0.5 V. This type of low power operation is an advantage of ionic liquid gate dielectrics transistors. The field effect mobility in the saturation regime is calculated as $\mu = 7.2 \times 10^{-4}$ cm^2 V^{-1} s^{-1}, using the equation 2.1, where *L*, *W*, and *C* are the channel length, the channel width, and the capacitance of the dielectric layer, respectively. The value of *C* for DEME-TFSI was obtained as 1 μFcm^{-2} in a separate measurement using a parallel plate capacitor of this material. The μ value of H_2TTDPz is nearly comparable to that of F_{16}MPc.[13]

$$\mu = \frac{2L}{WC}\left(\frac{\partial\sqrt{I_D}}{\partial V_G}\right)^2 \quad \text{(Eq.2.1)}$$

The obtained values for μ of H_2TTDPz are not very high, perhaps because of a mismatch between the conduction pathway and the π stacking direction, as indicated in Fig 2.9. Namely, the molecular planes of H_2TTDPz are parallel to substrates, so that π stacking does not bridge the distance between the source and drain electrodes. However, the *n*-type semiconductor behavior of H_2TTDPz indicates that *p*-*n* junctions between the series of Pc and H_2TTDPz would be highly possible, which are applicable to bulk heterojunction photovoltaic cells. Since porphyrazine has a good chemical and is useful in organic electronics, all porphyrazine-based organic devices would be promising.

2.6 Electrochemistry and Electrochemical Doping of H_2TTDPz Thin Films

2.6.1 Electrochemical Characterization

The cyclic voltammetry (CV) of H_2TTDPz films on ITO was measured in 0.1 mol dm^{-3} aqueous solutions of various electrolytes. H_2TTDPz films exhibited only a reduction peak, reflecting that this material is an acceptor having electronegative thiadiazole rings on its molecular skeleton. The repeatability of the redox cycle significantly depended on the electrolytes; the thin films exhibited a repeatable redox cycle in the solutions of KCl, NH_4Cl, etc., while they gradually dissolved or peeled off in the LiCl solution within a few cycles. Fig 2.12 depicts the CV curves in the aqueous solution of NH_4Cl. In the first cycle, a sharp reduction peak appeared at −0.23 V, but in the second or later cycles, the reduction took place at −0.12 V with good reproducibility. The CV peak shape in the first cycle was dependent on the area size of the ITO

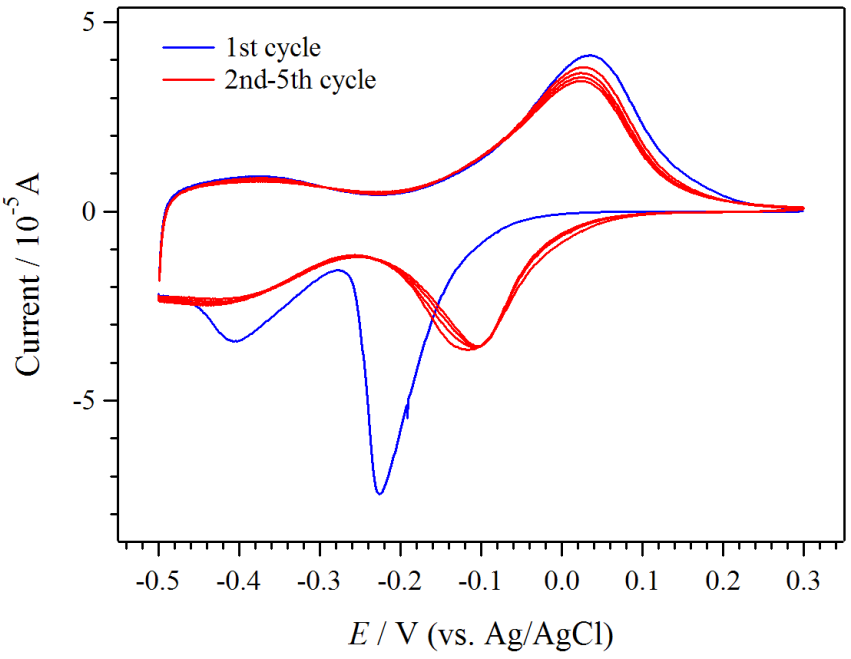

Figure 2.12 CV curves of H_2TTDPz thin film in the aqueous solution of NH_4Cl.

electrode; the peak became broader and/or split into two when larger electrodes were used. This type of overpotential, as compared to the peak position on all subsequent scans, was often observed in the various thin film samples, and was attributed to an irreversible penetration of counter ions into the film for charge balancing and/or a surface process such as film restructuring.[14–16] In the oxidation scans, on the other hand, an oxidation peak always appeared at 0.05 V.

The *n* values for the reductions of H_2TTDPz in the first and second cycles were determined to be 0.86 and 0.63, respectively, using chronocoulometry.[17] The difference between the two values is probably due to the fact that some of the counter cations (NH_4^+) that penetrated into the film in the reduction scan remained even after the oxidation scan. The *n* value for the oxidation was determined to be 0.70. This was in fairly good agreement with the value for the reduction in the second cycle. To support one-electron reduction, X-band electron paramagnetic resonance (EPR) was measured for reduced thin films at $E = -0.7$ V on ITO, after removing the samples from the solutions, rinsing with water, and then drying. Although the sample was exposed to air

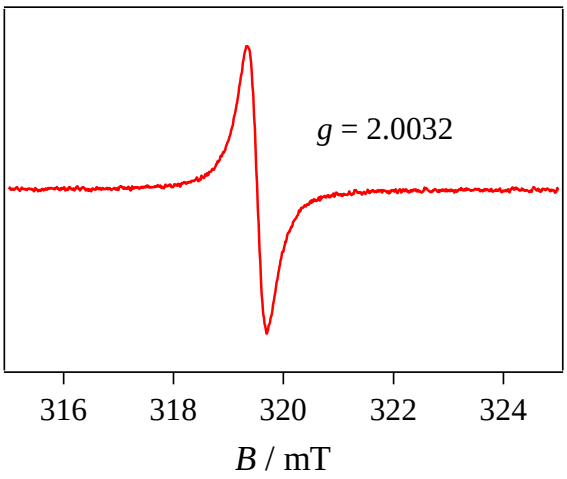

Figure 2.13 EPR spectrum of reduced H_2TTDPz thin film at room temperature.

once in these measurements, the color of the thin films indicated that H_2TTDPz was still in the reduced state (see Fig 2.14).

Fig 2.13 shows the EPR spectrum at room temperature. While the neutral thin film was EPR silent before reduction, a single-line absorption appeared at g = 2.0032, indicating the presence of an anion radical species, which was consistent with the results of the chronocoulometry. It is notable that this EPR signal was persistent even in air, indicating the stability of the anion radical of H_2TTDPz.

2.6.2 Optical Characterization

During the CV redox process, H_2TTDPz thin films underwent a significant color change. Fig 2.14 shows the photographs of the thin film in the KCl solution (0.1 mol dm^{-3}) at the three potentials. This material was initially light blue, and turned first to purple and then to brown during the reduction. This color change was reversible over many cycles, and was essentially independent from the electrolytes. Fig 2.15 depicts the *in-situ* absorption spectra in the NH_4Cl solution (0.1 mol dm^{-3}), indicating a systematic change with three isosbestic points. The presence of these points indicated the stability of this thin film upon reduction. Before reduction (E = 0 V), the so-called Q-band and

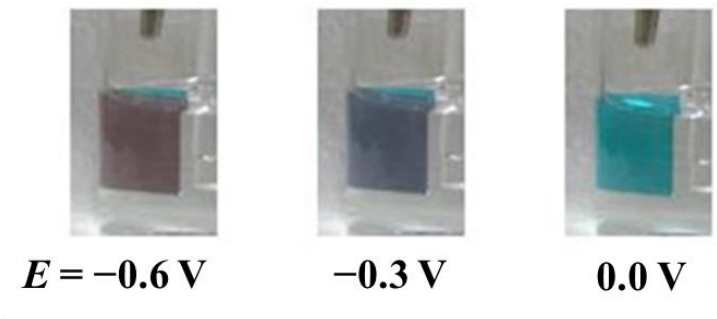

Figure 2.14 Photographs of the thin film in the KCl solution at three potentials.

Soret band appeared at 2.0 and 4.0 eV, respectively. With a decrease of the potential, new bands came out at 2.3 and 2.8 eV. Since their intensities were similar to that of the original Q-band, they can be ascribed to the bands of this character. The Soret band appeared to exhibit a high-energy shift after reduction. The new weak band at 1.3 eV is probably ascribable to an intermolecular charge-transfer (CT) band. The structure of the thin film is expected to include an interlayer π–π overlap, so that it would be reasonable to expect a magnification of CT after reduction. Upon oxidation, a reversible spectral change was observed. The black dotted curve shows the absorption of the oxidized sample at E = 0 V, which has experienced the potential of E = +0.2 V once. This curve is similar in features to that of the original sample, but does not agree with it completely. This suggests that a small number of the penetrated counter cations still remain even after the oxidation in the film.

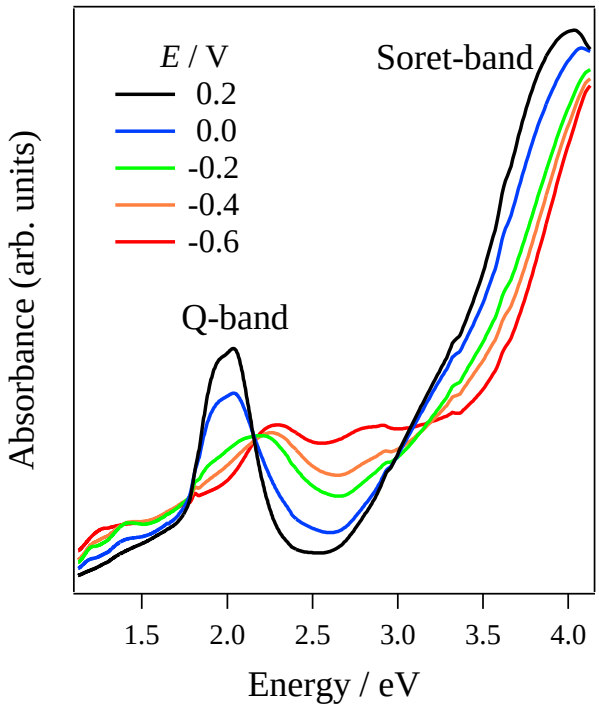

Figure 2.15 *In-situ* absorption spectra of H_2TTDPz thin film in the NH_4Cl solution during electrochemical processes.

2.6.3 Structural Analysis on Doped Thin Films

Fig. 2.16 shows the XRD pattern change of the H_2TTDPz thin film around 2θ = 27° in the redox cycle. These are not the results of *in-situ* measurements; XRD patterns were measured after removing the samples from the solutions, rinsing with water, and then drying. The black curve in Fig 2.16 shows the pattern of the original thin film, exhibiting a peak at 2θ = 27.3°. The red curve shows the results on the reduced one deposited at E= −0.5 V. The peak position was shifted to 27.5° with a significant decrease in intensity. The peak shift is small, but is larger than the experimental error. This is supported by the fact that the XRD peaks from ITO at 30.5° in the three curves are in precise agreement. The interlayer distance in the reduced thin film was calculated to be 0.325 nm, which is slightly shorter than that before reduction. This decrease in the interlayer distance is presumably caused by the CT interactions between anion radical species, suggested in the absorption spectra in Fig.

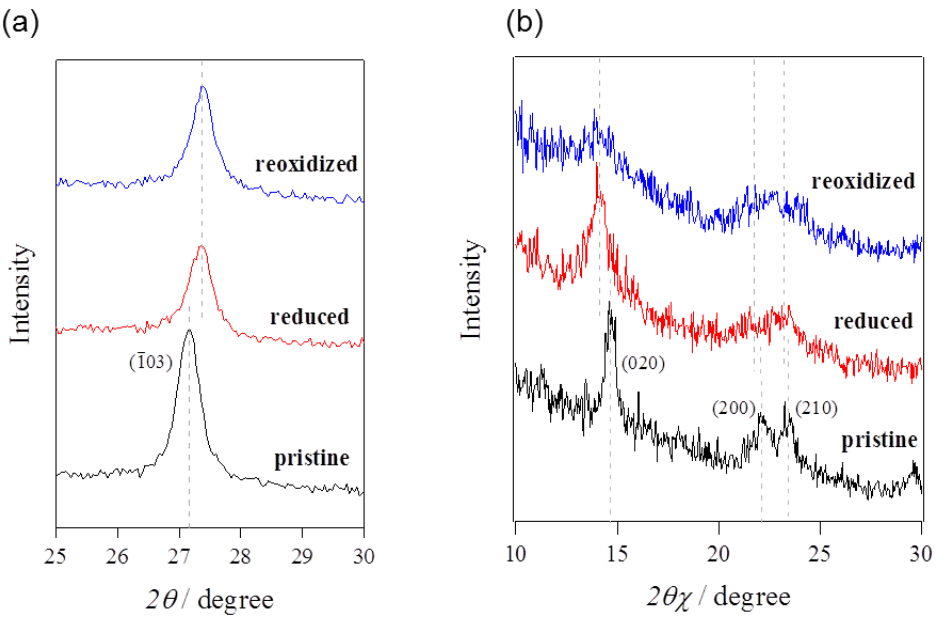

Figure 2.16 (a) Out-of-plane and (b) in-plane XRD pattern change of H_2TTDPz thin film around in the redox cycle.

2.15. The presence of a lamellar structure in the reduced thin film was unexpected, because thin film reduction (or oxidation) was believed to be accompanied by penetration of counter cations (or anions) into the films for charge balancing. The persistence of the lamellar structure in H_2TTDPz thin films is considered to be due to the strong self-assembling ability of this molecule. On the other hand, it was confirmed that the diffraction peaks of in-plane pattern shifted to larger inter-plane distance that was reverse to the tendency of out-of-plane diffraction pattern as shown in Fig. 2.16(b). This result indicates that mobile cations injected by the electrochemical doping exist out of the stacking axis rather than in the space between stacking molecules and therefore the steric hindrance by dopant cations may not have a significant effect on the carrier transport in the stacking direction. It is also considered that the counter cations, penetrated into the film, only break the in-plane structure and/or that the penetration depth of the cations is not very deep, and thus only breaks the structure in the vicinity of the surface.

The blue-curve sample was reset in the electrochemical cell and oxidized at E = 0.2 V. The blue curve in Fig 2.16 shows the XRD pattern of this thin film. Although the color and resistivity were nearly the same as those of the original thin film, the compressed structure was still maintained after oxidation. This is probably due to the remaining counter cations in the film.

2.6.4 Electrochemical Doping and *In-situ* Electrical Characterization

In-situ resistance measurements on the H_2TTDPz thin films were performed during the redox scan with the electrochemical apparatus depicted in Fig. 2.17, following the method reported in Ref 18. The gap width of the two-band electrodes (Pt)

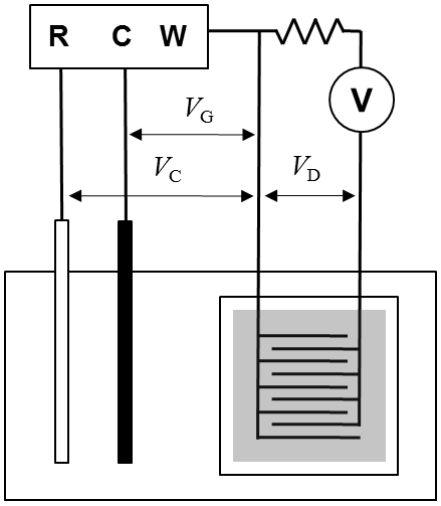

Figure 2.17 Electrochemical apparatus for *in-situ* resistance measurements on H_2TTDPz thin films.

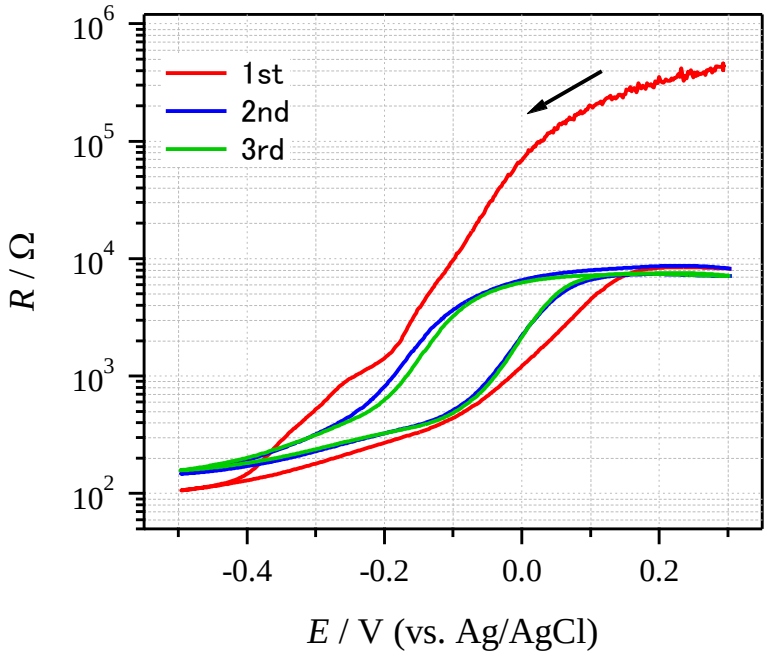

Figure 2.18 *In-situ* resistance of H_2TTDPz thin film vs voltage plot in the redox cycle.

was 2 μm, and the film thickness was 100 nm. This system of measurement resembles electrochemical transistor structure which was proposed by Wrighton *et al.*[18] Electrochamical doping was performed applying potential V_g on the Pt microelectrodes and the resistance of H_2TTDPz thin film was evaluated by recording conduction current in between microelectrodes during applying alternative voltage V_d of 10 mV. The results are shown in Fig 2.18. The resistance *R* of the initial thin film was in the order of 10^6 Ω in the NH_4Cl solution. Upon reduction, the *R* value suddenly decreased by three orders of magnitude at *E* = 0 V. Since this critical voltage is roughly coincident with the CV reduction peak (−0.15 V) in the second cycle or later, the enhancement of conductivity would have been caused by the generation of unpaired electrons that became charge carriers. Upon oxidation, an increase of *R* was found with a hysteresis which should be affected by the hysteresis in doping/dedoping redox curves. The *in-situ* resistance measurements clearly indicated an enhancement of conductivity at the reduction point. The electrochemical method can be utilized in the charge control of MTTDPz thin films, which is a key to obtaining the desired electrical properties.

2.7 Conclusion

In summary, we prepared thin films of H_2TTDPz with a thickness of 100 nm. They were found to include a high and unusual orientation of the molecular planes; the planes are all parallel to the substrate surface, reflecting the strong self-assembling ability of H_2TTDPz. The photocurrent and FET performance measurements on thin films of H_2TTDPz were performed and firm evidence of *n*-type semiconductor behavior was confirmed. The ITO/H_2TTDPz/Au cells exhibited symbatic and antibatic behavior,

according to bias voltage and illumination direction, which was well-interpreted as a filter effect for the *n*-type semiconductors. The H_2TTDPz FET showed a typical feature of *n*-type semiconductors. The electron mobility was evaluated from the transfer characteristics as μ = 7.2 × 10^{-4} cm^2 V^{-1} s^{-1}. The electrochemical reduction of H_2TTDPz thin films was observed at *ca*. −0.1 V vs. Ag/Ag^+, reflecting a high electron affinity of *n*-type semiconductor. This electrochemical doping with nearly one electron occurs accompanied by electrochromism, and enhanced intermolecular interactions were indicated by the presence of CT band after reduction. The XRD patterns exhibited that the lamellar structure of H_2TTDPz still remained even after the penetration of counter ions. As a result, H_2TTDPz thin films exhibited an enhancement of electrical conductivity by electrochemical doping.

References

1. M. Fujimori, Y. Suzuki, H. Yoshikawa, K. Awaga, *Angew. Chem. Int. Ed*. **2003**, *42*, 5863–5865.
2. Y. Suzuki, M. Fujimori, H. Yoshikawa, K. Awaga, *Chem. Eur. J*. **2004**, *10*, 5158–5164.
3. P. A. Stuzhin, E. M. Bauer, C. Ercolani, *Inorg. Chem*. **1998**, *37*, 1533–1539.
4. S. Heutz, T. S. Jones, *J. Appl. Phys*. **2002**, *92*, 3039–3046.
5. H. Ito, N. Nomura, T. Suzuki, S. Ukai, K. Marumoto, S. Kuroda, *Collid. Surf. A* **2006**, *284–285*, 613–616.
6. K. Kaneto, K. Takayama, W. Takashima, T. Endo, M. Rikukawa, *Jpn. J. Appl. Phys*. **2002**, *41*, 675–679.
7. A.K. Ghosh, T. Feng, *J. Appl. Phys*. **1978**, *49*, 5982–5989.

8. K. Yamashita, Y. Matsumura, Y. Harima, S. Miura, H. Suzuki, *Chem. Lett.* **1984**, *13*, 489–492.
9. Y. Harima, H. Okazaki, Y. Kunugi, K. Yamashita, H. Ishii, K. Seki, *Appl. Phys. Lett.* **1996**, *69*, 1059–1061.
10. G.D. Sharma, M. Roy, M.S. Roy, *Mater. Sci. Eng. B* **2003**, *104*, 15–25.
11. M.S. Roy, G.D. Sharma, S.K. Gupta, *Thin Solid Films* **1997**, *310*, 279–288.
12. Y. Tanaka, K. Takahashi, T. Kuzumaki, Y. Yamamoto, K. Hotta, A. Harasawa, Y. Miyoshi, H. Yoshikawa, Y. Ouchi, N. Ueno, K. Seki, K. Awaga, K. Sakamoto, *Phys. Rev. B* **2010**, *82*, 073408.
13. Z. Bao, A.J. Lovinger, J. Brown, *J. Am. Chem. Soc*. **1998**, *120*, 207–208.
14. J. L. Kahl, L. R. Faulkner, K. Dwarakanath, H. Tachikawa, *J. Am. Chem. Soc*. **1986**, *108*, 5434–5440.
15. K. L. Brown, H. A. Mottola, *Langmuir* **1998**, *14*, 3411–3417.
16. J. Silver, P. Lukes, A. Houlton, S. Howe, P. Hey, M. T. Ahmet, T. Mustafa, *J. Mater. Chem*. **1992**, *2*, 849–855.
17. "Methods for studies of electrochemical reactions": O. Hammerich in *Organic Electrochemistry, 4th ed*. **2001**, pp. 95–182.
18. E. W. Paul, A. J. Ricco, M. S. Wrighton, *J. Phys. Chem*. **1985**, *89*, 1441–1447.

Chapter 3. Electrochemical Doping of Lithium Phthalocyanine Thin Films

3.1 Introduction

In the last Chapter, we described the fundamental properties and the band filling control for the robust thin films of H_2TTDPz. A repeatable electrochemical doping with beautiful electrochromism and conductivity control, was realized, but this repetition gradually spoiled the crystallinity of the thin films due to penetration of counter cations into the thin films. These results motivated us to examine the band filling control to lithium phthalocyanine, which is described in Section 1.3.2. This is a well-known stable neutral radical, showing the crystalline polymorphs, α-, β- and x-forms.[1] The x-form consists of a 1D π stacking with a face-to-face intermolecular overlap, indicating a formation of 1D half-filled band. In between the stacking columns of x-LiPc, there is a 1D channel, whose size is comparable to the size of small molecules such as nitrogen and oxygen.[2] This feature indicates that the channels are capable of accommodating dopant ions, keeping the same packing of the LiPc molecules.

In Chapter 3, we describe the synthesis of LiPc, and its thin film fabrication and characterization. The solid-state electrochemistry of the thin films of LiPc is elucidated. We discuss a continuous electrochemical doping, a structural transformation, and effects of thin-film conductivity.

3.2 Synthesis

LiPc was synthesized according to literature procedures (Scheme 3.1).[3]

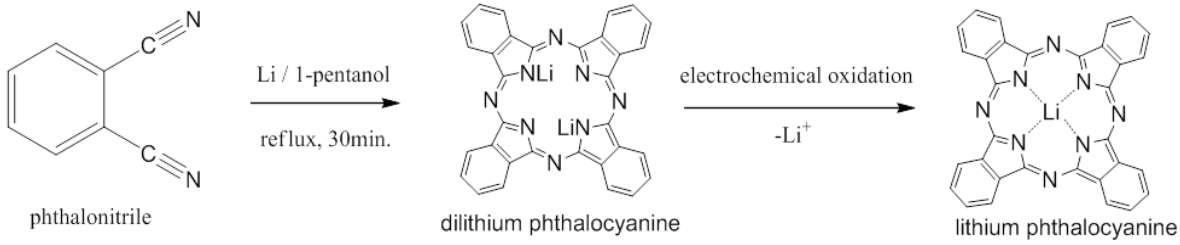

Scheme 3.1 Synthetic scheme of LiPc.

3.2.1 Dilithium Phthalocyanine (Li_2Pc)

0.2 g of Li metal was suspended in *n*-amyl alcohol and heated at 70°C for 30 min in nitrogen atmosphere. Then 3.0 g of phthalonitrile was added to the solution and refluxed for 1 hour. After evaporation of alcohol, precipitate was heated at 250˚C for 3 hours. Extracting the product with dehydrated acetone using Soxhlet extractor, the solution was condensed to *ca*. 20 mL. 100 mL of hexane was added to the solution. When dark green precipitate was formed, resulting Li_2Pc was filtered and dried under vacuum.

3.2.2 Lithium Phthalocyanine (LiPc)

LiPc has prepared by electrochemical oxidation of Li_2Pc with constant potential condition. In this electrochemical synthesis, tetrabuthylammonium perchlorate (TBAP) was used as a supporting electrolyte. TBAP was purified by recrystallization from the mixed solution of ethyl acetate and toluene prior to use, and dried under vacuum for at least one day. 100 mL of 0.1 mol dm^{-3} TBAP/acetonitrle solution and 200

mg of Li_2Pc was added to an electrochemical cell. The above setup of the electrochemical cell was prepared under nitrogen atmosphere to avoid the contamination by water and oxygen in air. After confirming the dissolution of all reagents, the electrolysis started. It takes about 6 hours to oxidize the all Li_2Pc. Since the LiPc is insoluble in acetonitrile, the crystalline LiPc has formed on the platinum electrode. The resulting crystals of LiPc were collected by filtration and washed with abundant acetonitrile and then dried under vacuum to obtain needle shaped green crystals.

3.3 Fabrication and Characterization of Thin Films

LiPc thin films of 120 nm in thickness were prepared on ITO substrates by vacuum vapor-deposition at 480°C. The obtained thin films were determined to have the

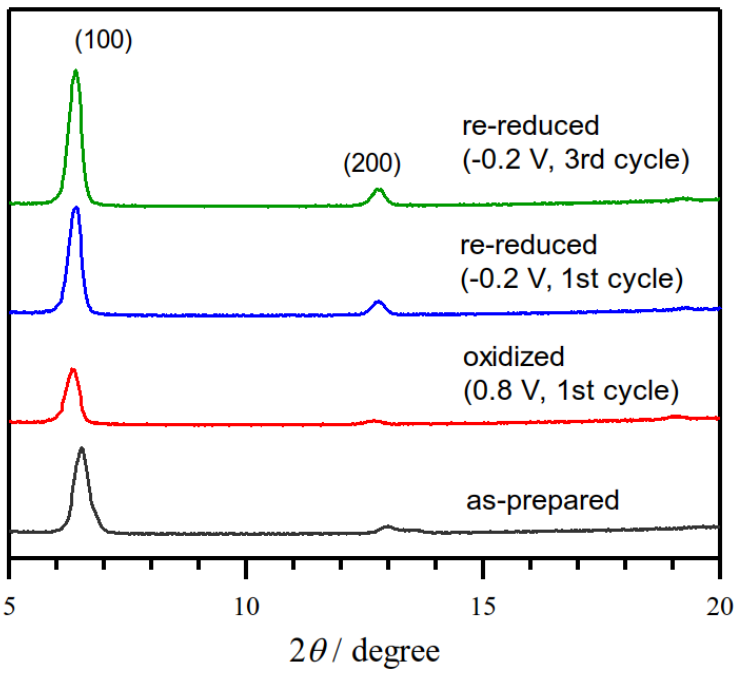

Figure 3.1 XRD patterns of LiPc thin film in the redox process.

α-form by X-ray diffraction (XRD) and absorption spectra. The black curve in Fig. 3.1 shows the XRD pattern ($2\theta/\theta$ scan), showing weak peaks at 2θ = 6.7 and 13.11. This pattern corresponds to an interplane distance of 13.4 Å, which is nearly in agreement with the reported value for the α-form.[4] The formation of the α-form is further supported by the UV-Vis-NIR absorption spectra measurements as described later.

3.4 Electrochemical Characterization

Cyclic voltammetry (CV) measurements of the α-form LiPc films on ITO were made in 0.3 mol/dm^3 acetonitrile solutions of various electrolytes. The thin films exhibited a repeatable redox cycle in solutions of $N(C_4H_9)_4ClO_4$ (abbreviated as TBAP), $N(C_4H_9)_4BF_4$ and $LiClO_4$. Fig. 3.2 depicts the CV curves for the first three cycles in an acetonitrile solution of TBAP. In the first cycle (black curve), an oxidation peak appears

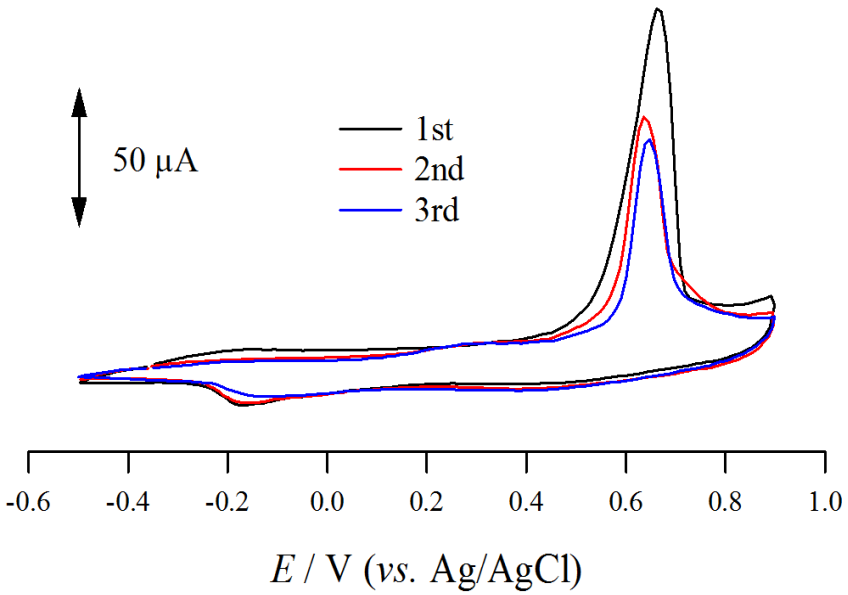

Figure 3.2 CV curves of LiPc thin film for the first three cycles in an acetonitrile solution of TBAP.

at E = 0.66 V. As shown later, this oxidation process is associated with a significant color change and penetration of the counter anions (ClO_4^-) in the thin films to balance the charge. In contrast, there is no sharp peak in the re-reduction scan from 0.9 to 0.5 V, though this also exhibits a gradual color change. The second (red curve) and third (blue curve) cycles show oxidation peaks at 0.64 V with a decrease in peak intensity. Note that, after the third cycle, there is a good reproducibility of the CV curve, as is found in the second and third cycles. The anomaly of the first cycle is probably caused by an overpotential effect and/or the presence of irremovable counter anions in the thin films after the second cycle.[5,6]

3.5 Structural Analysis on Doped Thin Films

The red and blue curves in Fig. 3.1 show the XRD pattern change in the electrochemical redox cycle. These are not the results of *in-situ* measurements; we measured the XRD patterns after removing the samples from the solutions, rinsing with acetonitrile, and then drying. The red curve shows the results for the oxidized sample deposited at E = 0.8 V. Unexpectedly, this curve shows two strong peaks at 2θ = 6.4° and 12.8° with a significant increase in signal intensity. These indicate a structural modification and an improvement in the crystallinity of the thin film after oxidation. The corresponding d value is 13.9 Å, which is in good agreement with that of the x-form.[4] The blue curve shows the results at E = 0.2 V. There is little change from the red curve, meaning that the x-form structure is maintained after re-reduction.

In the course of the solid-state electrochemical reactions, the LiPc thin films exhibited a significant electrochromism, as shown in the inset of Fig. 3.3. We measured

in-situ UV-Vis-NIR absorption spectra. The black curve in Fig. 3.3(a) shows the spectrum for the as-prepared thin film of LiPc soaked in acetonitrile. This curve exhibits characteristic features of the α-form, namely, broad twin peaks in the range of 600–800 nm and a small peak at 820 nm.[4,7] This figure also shows the spectral change in the first oxidation scan at E = 0.2, 0.6 and 0.9 V. While there is a gradual change in the visible range (400–700 nm) with an isosbestic point at 580 nm, the weak absorption at 820 nm suddenly disappears at E = 0.9 V, where the spectrum consists of two sharp bands at 520 and 690 nm. Fig. 3.3(b) depicts the results in the first re-reduction scan from 0.9 to 0.2 V; the two sharp peaks exhibit high-energy shifts, swapping their intensities. At −0.2 V, namely after the first redox cycle, the spectrum is completely different from the original

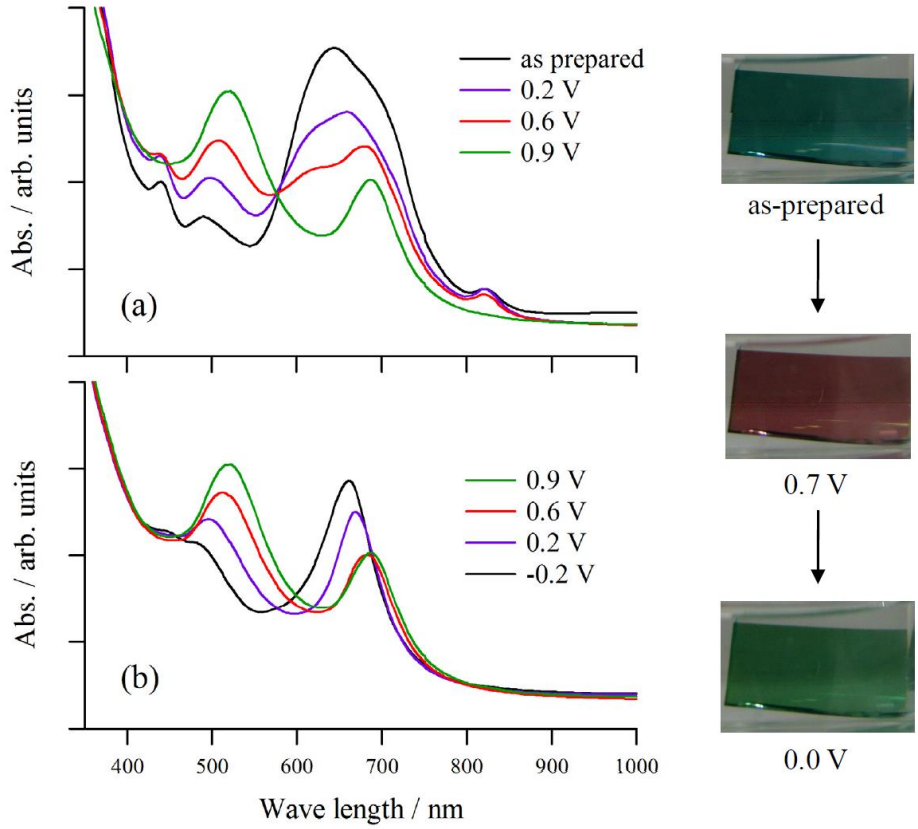

Figure 3.3 UV-Vis-NIR absorption spectra of LiPc thin film in the redox process. (a) oxidation and (b) reduction process (Inset: photograph of thin film).

one (black curve in Fig. 3.3(a)), and is identical with that of the x-form.[4,8] In the second cycle or later, the spectral change becomes reversible; it repeats the change in Fig. 3.3(b).

X-ray photoelectron spectra (XPS) measurements were carried out for the as-prepared thin film, and the oxidized (E = 0.8 V) and re-reduced (E = 0.2 V) films in TBAP/acetonitrile solution. The sample preparations for these measurements were the same as those for the XRD measurements. Fig. 3.4(a) shows the Li 1s bands for the three samples. The as-prepared sample exhibits a signal at a binding energy of 58 eV (black curve), which is shifted to 56 eV after oxidation (red curve) and reverts to the original position (59 eV) after re-reduction (blue curve). Since there is little change in

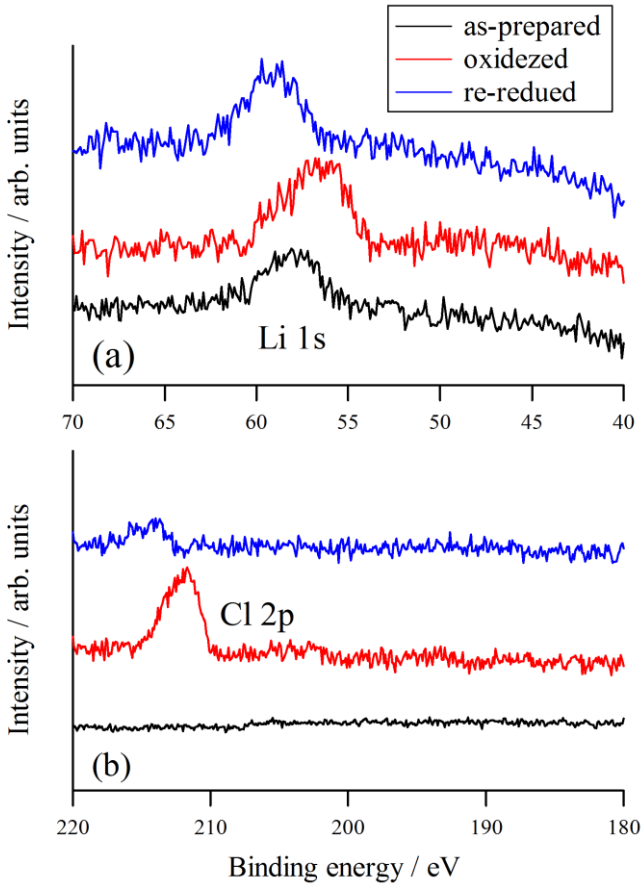

Figure 3.4 XPS spectra of LiPc thin film in the redox cycle for Li (a) and Cl (b).

signal intensity, there should be no elimination of Li ions from LiPc molecules. Fig. 3.4(b) depicts the spectra of Cl 2p. While the as-prepared thin film exhibits no signal of Cl (black curve), the oxidized film does exhibit a strong peak at 212 eV (red curve). This is firm evidence for doping of the counter anion (ClO_4^-) into the thin film after oxidation. After re-reduction, however, this peak nearly disappears (blue curve), due to dedoping. The presence of the weak peak on the blue curve suggests that a small amount of ClO_4^- remains even after re-reduction.

Scheme 3.2 shows a summary of the present work. The α-form thin films of LiPc exhibit a structural transition to the x-form as a result of electrochemical oxidation, which brings about doping of the counter anions into the thin films. This process is followed by reversible dedoping, which occurs with maintenance of the same crystal structure by electrochemical re-reduction. Since the x-form crystals of the cation radical salts of divalent phthalocyanines, (MPc)X (M = Ni, Pt,etc. and X = ClO_4, BF_4, etc.), are

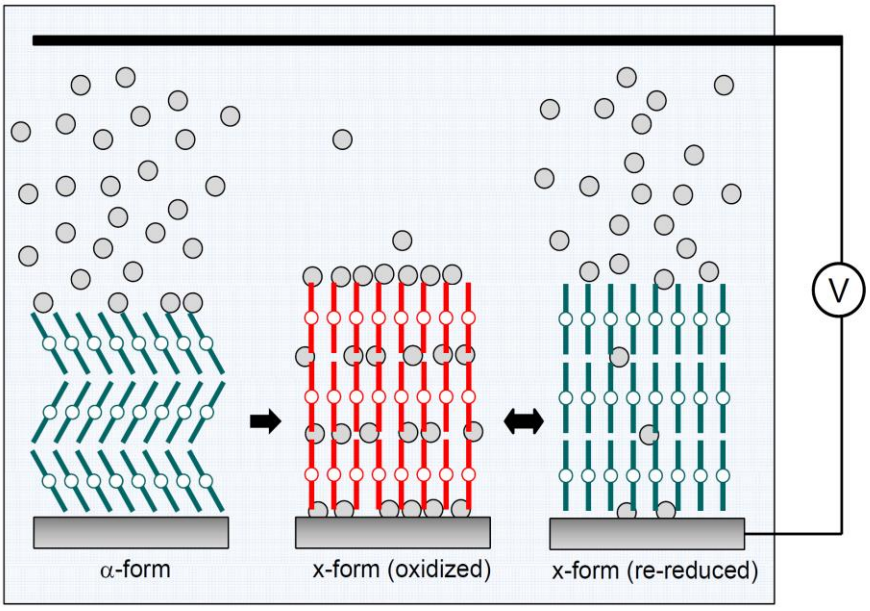

Scheme 3.2 Schematic view of electrochemical doping process of LiPc thin film.

synthesized electrochemically,[9] the present α→x transformation of the LiPc thin films can be regarded as a solid-state reaction, rather than a phase transition. In our previous work, however, it was demonstrated that electrochemical oxidation of "the α-form thin films of divalent MPc did not bring about formation of the x-form, but an amorphous structure. This is a clear contrast between LiPc and divalent MPc; LiPc can stably form the x-form even without counter anions. Furthermore, the doped anions in the oxidized state of LiPc are easily dedoped by electrochemical re-reduction, maintaining the x-form structure. While reversible I_2 doping and thermal dedoping are known in powder samples of a Pc polymer $[SiPcO]_n$,[10] the present electrochemical method can provide highly-controllable doping/dedoping. The structural robustness of the x-form LiPc thin films is probably attributable to the fact that LiPc is a neutral radical which possesses strong intermolecular radical–radical interactions and to the presence of the 1D channels, which can be a pathway for counter anions.

3.6 Electrochemical Doping and Electrical Transport Properties of Thin Films

The repeatability of the redox cycle after the second cycle strongly suggests a possible electrochemical band-filling control, namely, continuous and reversible doping/dedoping in the same lattice skeleton, by means of electrochemistry.

Substrates and electrodes used for this experiment were the same as those in H_2TTDPz (section 2.5.4). The electrochemical potential swept from 0.0 V to 0.9 V at a sweep rate of 5 mV/s. After this 1st oxidation process, the sweep stopped at each desired potential in the 1st backward scan. After confirming electrochemical equilibria, thin films were rinsed with acetonitrile and transferred to a cryostat. Electrical measurements were performed in nitrogen atmosphere. Fig. 3.5 shows the temperature

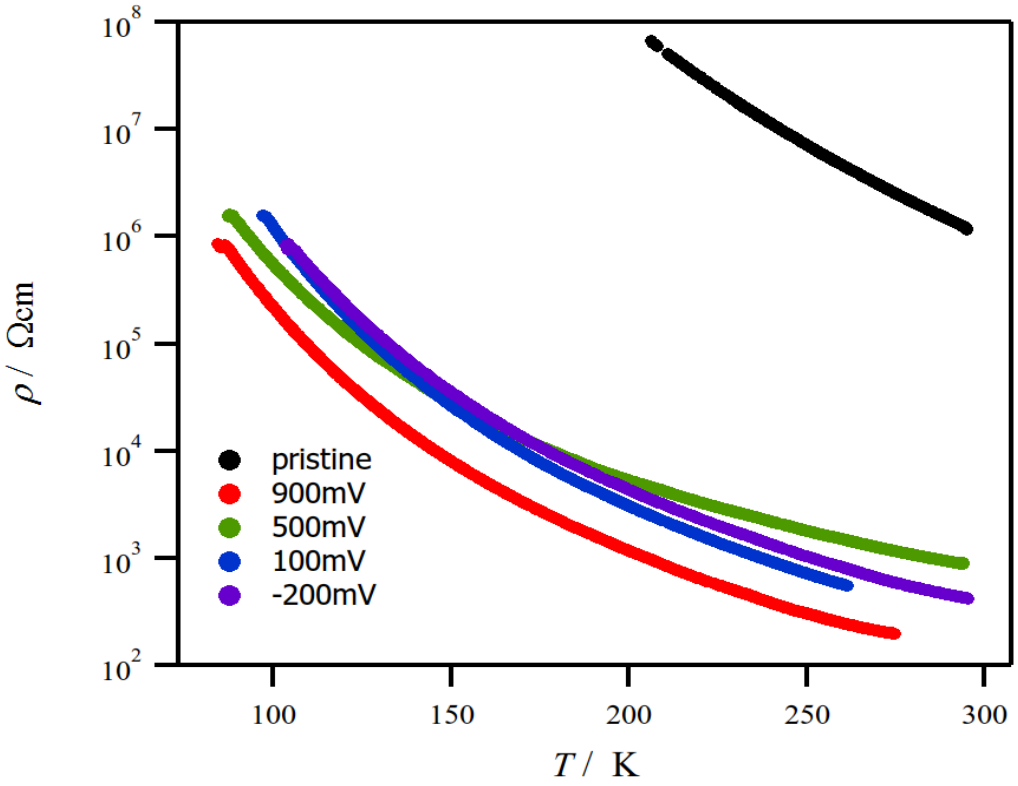

Figure 3.5 Temperature dependence of electrical resistivity on LiPc thin films doped at each electrochemical potential, 0.9 V, 0.5 V, 0.1 V, and −0.2 V.

dependence of electrical resistivity on LiPc thin films doped at each electrochemical potential, 0.9 V, 0.5 V, 0.1 V, and −0.2 V. It is clear that due to effective carrier injections, all the doped LiPc thin films exhibited lower resistivity by 2–3 orders of magnitude than pristine film. It is worth noting that there was only a small variation, less than one order of magnitude, in between resistivities of doped thin films. This result imply that the resistivity of LiPc thin films did not exhibit an intrinsic property of bulk thin film, but an electrically conductive fraction in thin films governed electrical transport. This behavior was interpreted by the presence of immobile dopant ions resulted from incomplete and inhomogeneous dedoping process as suggested by the results of XPS measurements.

3.7 Conclusion

In summary, we prepared the α-form thin films (120 nm) of lithium phthalocyanine (LiPc). They exhibited a structural transformation to the x-form by electrochemical oxidation which introduces the counter anions into the thin films, and these anions are reversibly dedoped by electrochemical re-reduction, maintaining the x-form structure. Electrical resistivity measurements on the LiPc thin films by electrochemical doping demonstrated that all the doped LiPc thin films exhibited lower resistivity by 2–3 orders of magnitude than pristine film. This result indicates that an electrically conductive fraction in thin films governed electrical transport.

References

1. M. Brinkmann, P. Turek, J.-J. Andre, *J. Mater. Chem*. **1998**, *8*, 675–685.
2. F. Bensebaa, J.-J. Andre, *J. Phys. Chem*. **1992**, *96*, 5739–5745.
3. H. Sugimoto, T. Higashi, M. Mori, *J. Chem. Soc., Chem. Commun*. **1983**, 622–623.
4. M. Brinkmann, J. C. Wittmann, C. Chaumon, J.-J. Andre, *Thin Solid Films* **1997**, *292*, 192–203.
5. M. Kalaji, L. M. Peter, L. M. Abrantes, J. S. Mesquita, *J. Electroanal. Chem*. **1989**, *274*, 289–295.
6. C. Barbero, R. Kötz, M. Kalaji, L. Nyholm, L. M. Peter, *Synth. Met.* **1993**, *55–57*, 1545–1551.
7. H. Yanagi, A. Manivannan, *Thin Solid Films* **2001**,*393*, 28–33
8. H. Homborg, C. L. Teske, *Z. Anorg. Allg. Chem*. **1985**, 45–61.
9. J. L. Petersen, C. S. Schramm, D. R. Stojakovic, B. M. Hoffman, T. J. Marks, *J. Am.*

Chem. Soc. **1977**, *99*, 286–288.

10. T. J. Marks, *Angew. Chem., Int. Ed*. **1990**, *29*, 857–879.

Chapter 4. Electrochemical Doping of Lithium Phthalocyanine Crystals

4.1 Introduction

In Chapter 3, we described the reversible electrochemical doping/dedoping to the thin films of LiPc. Owing to the nanoporous structure of this compound, controllable doping/dedoping were realized, keeping the crystallinity stable. However, the conductivity measurements on these LiPc thin films suggested an inhomogeneity of the counter anions in the films, which resulted in a discontinuous change, as shown in Section 3.6. To achieve the ideal band filling control, it is necessary to perform continuous carrier doping/dedoping in single crystals organic semiconductors.

In the present chapter, we explain an electrochemical doping to the single crystals of LiPc, by a successive electrochemical method: namely the electrochemical growth of the single crystals of LiPc, followed by electrochemical doping, using two kinds of electrochemical cells. Crystal structure analysis on the crystals of different doping levels, reveal homogeneous distributions of the counter anions in the crystals. Electrical measurements suggest a continuous enhancement of conductivity by a decrease in carrier number from the half-filled band.

4.2 Preparation of Electrochemically Doped LiPc Crystals

LiPc crystals were grown on an electrode by electrochemical oxidation of Li_2Pc with a constant current condition. In this electrochemical synthesis, we used an H-shaped glass cell, consisting of anode and cathode compartments. They were separated from each other by a glass filter (pore size: 40–50 μm) to control diffusion speed. Platinum rods with a diameter of 1 mm were used as electrodes, and tetrabutylammonium perchlorate (TBAP) was done as a supporting electrolyte. TBAP was purified by recrystallization from a mixed solution of ethyl acetate and toluene prior to use, and dried under vacuum for at least one day. 100 mg of TBAP and 8 mL of acetonitrile were added to the each compartment, and 20 mg of Li_2Pc was added to the anode side. This electrochemical cell was set under nitrogen atmosphere, to prevent contaminations of water and oxygen from the air. After dissolving all reagents, the electrolysis was started. It took 3–4 weeks to oxidize all Li_2Pc in the solution. Since LiPc was insoluble in acetonitrile, the crystalline LiPc (dark green needle-shaped crystals, 0.2–1.0 mm in length) was grown on the surface of the platinum anode. The resulting LiPc crystals on the electrode were washed with acetonitrile three times, without peeling off from it, and then dried in air.

The electrochemical doping was carried out using another electrochemical cell as shown in Fig. 4.1, which had a three electrode structure. The platinum electrode covered with the LiPc crystals was used as a working electrode, and an Ag/Ag^+ electrode (BAS Co., Ltd.) and a platinum electrode (1 mm in diameter) were used as reference and counter electrodes, respectively. All the electrochemical reactions were performed under nitrogen atmosphere.

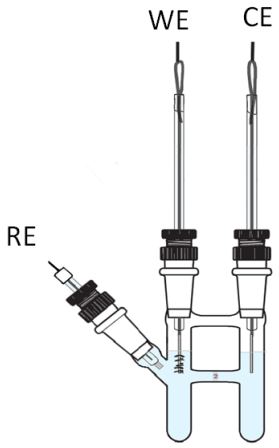

Figure 4.1 Electrochemical cell used for electrochemical doping.

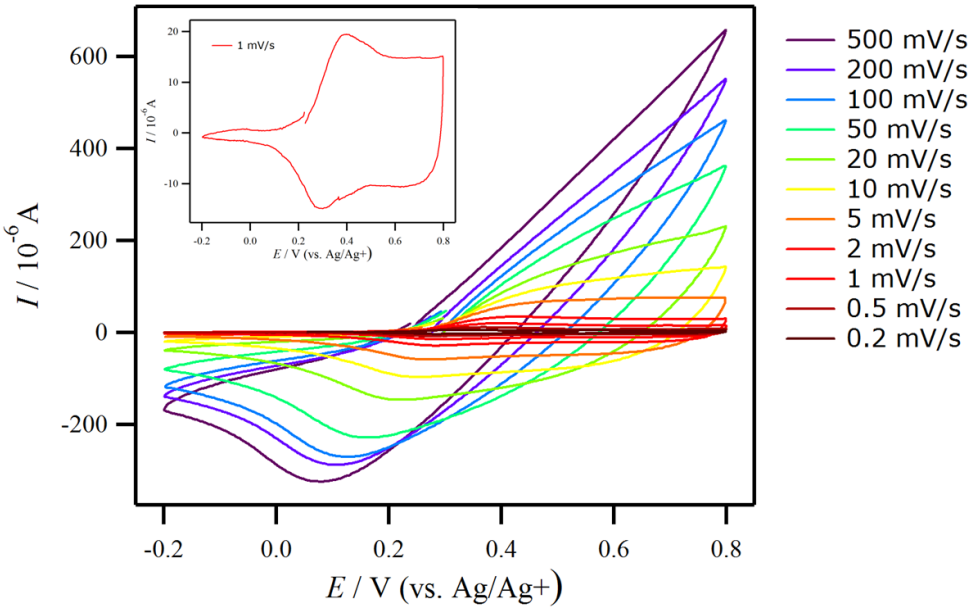

Figure 4.2 Cyclic voltammogram of LiPc crystals measured in 0.1 mol dm^{-3} acetonitrile solution of tetrabutylammonium chloride.

Fig. 4.2 shows a cyclic voltammogram of the LiPc crystals measured in a 0.1 mol dm^{-3} acetonitrile solution of tetrabutylammonium chloride (TBACl). Anodic and cathodic current peaks show significant shifts, depending on the scan rate. At a high

scan rate, the redox reaction is irreversible, and the potential difference between the anodic and cathodic peaks reaches 400 mV. In general, reversibility of the cyclic voltammograms for redox reactions is governed by a diffusion rate of reactants (redox species). In the present case, however, the reactants (LiPc molecules) were fixed on the surface of a working electrode, so that the reaction kinetics was not affected by diffusions of reactants. Instead, a diffusion rate of counter anions was a crucial factor to determine the reaction rate, because an electric charge should be compensated by a diffusion of anions into the crystals of the oxidized LiPcs.[1–3] Thus, the irreversible behavior of cyclic voltammograms at a high scan rates indicates a slow diffusion of counter anions. In contrast, the potential difference between anodic and cathodic peaks is as small as *ca*. 80 mV when a scan rate is less than 1 mVs^{-1}. This value is similar to a theoretical one in a reversible system (57 mV at room temperature), and therefore the cyclic voltammograms at a slow scan rates (< 1 mVs^{-1}) can be regarded as a quasi-reversible system.

To perform electrochemical doping into the LiPc crystals, a constant potential was applied to a 0.1 mol dm^{-3} TBACl/acetonitrile solution. Fig. 4.3 shows the time trajectory of the oxidation current during the electrochemical doping at 0.3, 0.4 and 0.5 V. When the LiPc crystals are oxidized at 0.3 V (blue curve), the oxidation current shows a decrease with an insertion of the counter anions (chloride ions) into the crystals, and the current become nearly zero after reaching an electrochemical equilibrium state within several hours. When the crystals are oxidized at 0.4 V (green curve), a current value is large at the beginning, and then decreases more quickly, compared to the current decay measured at 0.3 V. It should be noted that the time required completing the doping exhibited significant sample dependence, even though all samples had been

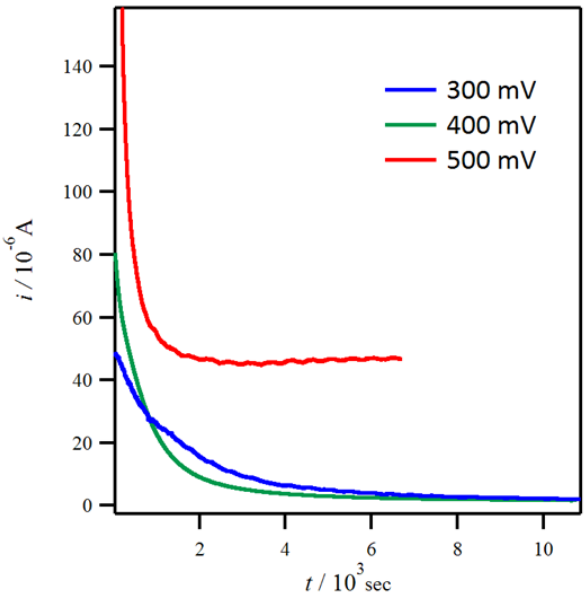

Figure 4.3 Plot of oxidation currents vs. time during the electrochemical doping at various potentials.

prepared under the same condition. In fact, the crystals used for the experiment had a size distribution. The size and the shape of crystals synthesized by the electrochemical method, are known to be strongly influenced by various factors such as electrode surface condition and electrolyte concentration. It is considered that the difference between the blue and green curves in Fig. 4.3, would be caused by the size and the shape of crystals deposited on the electrode, and the surface area between crystals and electrolyte solution would also affect the electrochemical behavior. A doping level can be estimated from the amount of the electric charges, consumed for the oxidation, and the mass of the materials on the electrode. However, in the present experiments, it was hard to do so, because a part of the crystals fell down from the electrode during or after the doping.

When the crystals are oxidized at 0.5 V, the electrolysis curve (red curve in Fig. 4.3) greatly differs from the other two. The values of the current decrease at the

beginning, but reach at a non-zero value afer 2000 sec. In this steady state, the oxidation reactions took place not for LiPcs but for the chloride ions in the electrolyte solution. It was confirmed by a control experiment that the electrolyte solution (0.1 mol dm^{-3} TBACl/acetonitrile) was oxidized continuously using bare platinum electrodes above *ca*. 0.5 V vs. Ag/Ag^{+}. Therefore, in order to avoid the decomposition of the electrolyte, the doping was performed at a potential below 0.5 V.

4.3 Characterization of Electrochemically Doped LiPc Crystals

It is expected that the concentration of the chloride ions, contained in electrochemically-doped LiPc crystals, would depend on the doping potential, under the guidance of the Nernst equation. Energy dispersive X-ray analysis (EDX) was performed on the obtained samples, in order to confirm the presence of chloride ions in them.

The samples obtained by the electrochemical dopings were firstly rinsed with pure acetonitrile three times for a few seconds to remove excess electrolyte remained on crystal surfaces. After the LiPc crystals were collected from the platinum electrodes, elemental analysis was carried out using a scanning electron microscope (SEM) equipped with an EDX analyzer.

The results of the EDX analysis indicated the presence of the chloride ion and all the elements of LiPc in the doped crystals, though we could not detect hydrogen and lithium atoms due to their small electron densities. The concentration of the chloride ions was calculated from the atomic ratio of Cl:N from the EDX measurements. Fig. 4.4 shows the dependence of the dopant concentration *x* on the doping potential. Each open circle in this figure represents the concentration of chloride ions obtained from one

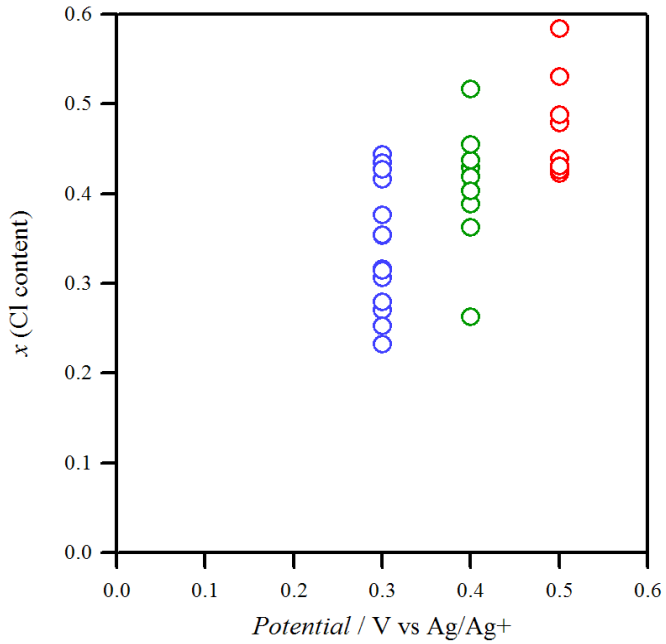

Figure 4.4 Relationship between a dopant concentration *x* and doping potentials.

piece of crystal, and the plots at each potential come from the same batch. It is clear that the carrier doping can be achieved by the electrochemical doping to the rigid single crystals of LiPc. One may suspect a contamination of the electrolyte molecules (TBACl), remained on sample surfaces, but this is not the case, because chloride ions were not detected from the LiPc crystals, which were just soaked in the electrolyte solutions without voltage, and were rinsed with acetonitrile, prior to EDX measurements.

Fig. 4.4 indicates that the concentration of chloride ions shows an increase, as the applied potential to the working electrode increases. The dopant level reaches the maximum (0.5), but further Cl doping has not been achieved, because the electrode potential above 0.5 V resulted in the decomposition of the electrolytes. A significant fluctuation is also observed even at the same potential, and this feature is common to the crystals at the three potentials (0.3 V, 0.4 V, and 0.5 V). These deviations are greater

than an experimental error of the EDX measurements, which is as large as *ca*. ± 0.1 from the average value. The Nernst equation for redox reactions indicates that the dopant concentration is determined by the doping potential. Therefore, the large distribution of *x* in the present materials suggests that an effective electric potential differs from crystal to crystal, even though they were on the same electrode. The resistivity of the neutral LiPc single crystals is about 10^5 Ω, which is extraordinarily large in the equivalent circuit of the electrochemical cell. When two or more single crystals contact each other on the electrode, there should be a significant potential drop at these crystals.

Fig. 4.5 shows an SEM image of a typical LiPc single crystal prepared at 0.3 V. This crystal was used for an EDX mapping analysis, in which we carried out EDX analysis at the five spots indicated by yellow circles in this figure. It was found that the chloride concentrations obtained from these spots were about 0.3 and there was no spot depeneence. Compared with the large fluctuation of the dopant concentration among the crystals (Fig. 4.4), the distribution of *x* in the same single crystal is probably very small, indicating a homogeneous distribution of the chloride ions.

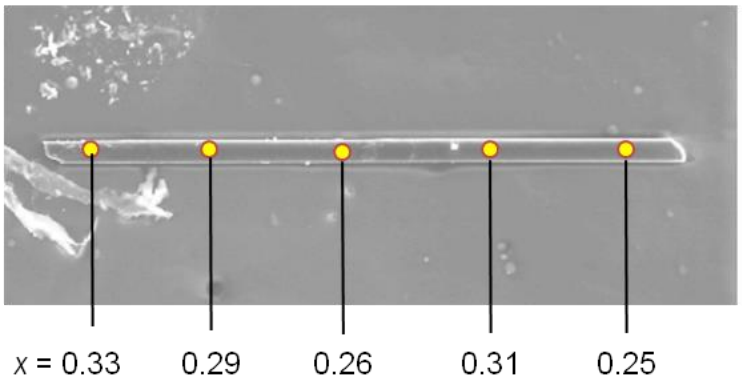

Figure 4.5 SEM image of a typical LiPc single crystal prepared at 0.3 V, used for an EDX mapping analysis. The values of *x* indicate a dopant concentration at the yellow points in the crystal, estimated from EDX analyses.

4.4 X-ray Crystal Structures of $LiPcCl_x$ Crystals

Detailed structural information for the $LiPcCl_x$ crystals was obtained by X-ray single crystal structure analysis. Since there was no chemical decomposition of the LiPc molecules after the electrochemical doping, it was able to perform a single crystal X-ray structure analysis on the doped crystals. The crystal structure was solved by a direct method using the SHELXS-97 program[4] and refined by successive differential Fourier syntheses and a full-matrix least-squares procedure using the SHELXL-97 program.[5] The occupancy parameters of the dopant (chloride ion) were refined isotropically at first. Then, the optimized occupancy was fixed to give the smallest *R* value, and finally chlorine atoms were refined anisotropically. Anisotropic thermal factors were applied to all non-hydrogen atoms. Hydrogen atoms in LiPc were located by differential Fourier synthesis and were also refined. In this work, the Cl occupancy was defined as the dopant concentration *x*. Table 4.1 summarizes the crystallographic data for the selected crystals with various dopant concentrations.

Table 4.1 Crystallographic data for the selected crystals with various dopant concentrations as well as a pristine x-form LiPc crystal.

Compound	x-LiPc	$LiPcCl_{0.11}$	$LiPcCl_{0.20}$	$LiPcCl_{0.21}$	$LiPcCl_{0.23}$	$LiPcCl_{0.39}$
Crystal system	tetragonal	tetragonal	tetragonal	tetragonal	tetragonal	tetragonal
Space group	*P*4/*mcc*	*P*4/*mcc*	*P*4/*mcc*	*P*4/*mcc*	*P*4/*mcc*	*P*4/*mcc*
a (Å)	13.852(4)	13.8430(9)	13.829(5)	13.864(6)	13841(4)	13.843(4)
c (Å)	6.4216(17)	6.4156(6)	6.406(2)	6.414(3)	6.4027(18)	6.394(2)
Volume ($Å^3$)	1232.2(6)	1229.41(16)	1225.1(7)	1232.8(9)	1226.6(6)	1225.3(6)
Z	2	2	2	2	2	2

The crystals analyzed here were electrochemically doped at the potential of 0.3 V, 0.4 V, or 0.5 V. The dopant concentration changed from crystal to crystal, being in the range of $0.1 < x < 0.5$ for $LiPcCl_x$. This is in agreement with the EDX analyses. The X-ray crystal structure analysis indicate that the $LiPcCl_x$ series are isostructural to the parent x-form LiPc,[6] except that chloride ions exist in the 1D channels. The crystal structure of $LiPcCl_x$ with $x = 0.37$, is shown in Fig. 4.6. The lithium ion is located at the center of the inner four nitrogen atoms of a planar phthalocyanine molecule. These LiPc

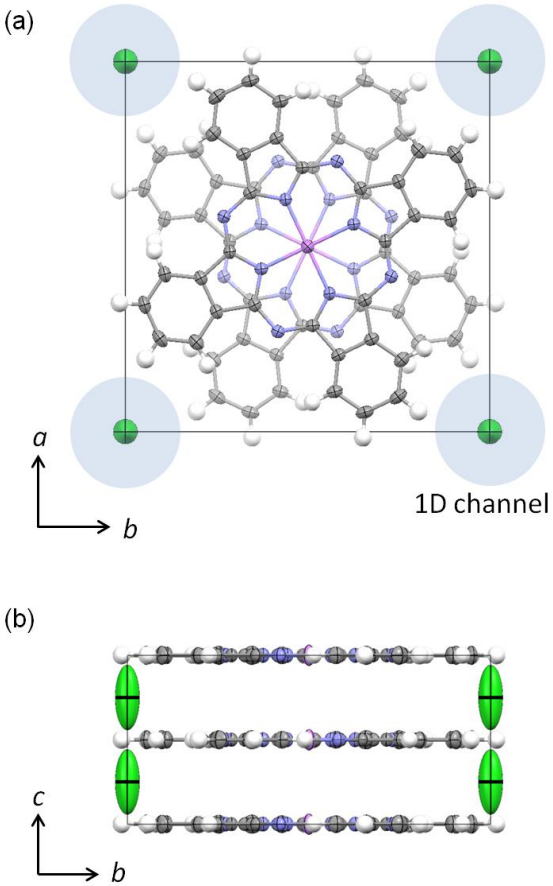

Figure 4.6 Crystal structure of $LiPcCl_{0.37}$. (a) the projection on the *ab* plane, (b) the projection on the *bc* plane. Green: Cl, Purple: Li, Violet: N, Gray: C, White: H.

molecules are stacked metal-over-metal so that their molecular planes are perpendicular to the *c* axis and are staggered by ca 39.1°. The interplanar spacing (*c*/2) is 3.1934(5) Å at 173 K, which is shorter than that in the LiPc crystal (3.2108(9) at 173 K). The chloride ions occupy a vacant space in the 1D channel as shown in Fig. 4.6. The thermal parameter of chloride ion in the stacking direction (*c* axis) is 7–10 times greater than those in the transverse directions (*a* and *b* axis), suggesting Cl disorder along the *c* axis as shown in Fig. 4.6(b). This is not surprising because there is enough space for Cl translation along the *c* axis, considering the non-commensurate character of $LiPcCl_x$ crystals. Similar behavior has been reported in $\{[Si(Pc)O]X_y\}_n$ and $M(Pc)X_y$ systems.[7,8]

Marks *et al*. argued about the relationship between the maximum dopant concentration and the size of counter ion in the $\{[Si(Pc)O]X_y\}_n$ system, where BF_4^-, PF_6^-, SO_4^{2-}, etc. were studied as a dopant.[9] Since the diameters of these counter anions (6.30–15.7 Å) are larger than the interplanar distance of the silicon phthalocyanine polymer (3.29–3.34 Å), the maximum dopant concentration was restricted, and was theoretically calculated as $y_{max} = d/2r_{ion}$, where d (= c/2) and r_{ion} are the interplanar spacing and the radius of counter ions, respectively. The maximum dopant concentration determined by the experiments for these ions, was ranged from 0.2 to 0.5, and indeed these values are in very good agreement with the theoretical ones. For the crystals of $LiPcCl_x$, the maximum dopant concentration can be theoretically estimated in the same way. Although the interplanar spacing of $LiPcCl_x$ is comparable with that of $\{[Si(Pc)O]X_y\}_n$ (3.23 Å at 273 K), the size of chloride ion ($2r_{ion}$ = 3.34 Å) is much smaller than those of the ions examined by Marks *et al*. By using these parameters, the theoretical value is obtained as 0.97, which indicates possible 1:1 complex of LiPc and Cl. However, the maximum dopant concentration obtained in the present work, is

smaller than 0.5. This suggests that the dopant concentration is restricted by the doping potential rather than the ion size in the $LiPcCl_x$ system.

Fig. 4.7 shows the dependence of the lattice constants *a* and *c* on the concentration *x* in $LiPcCl_x$. With an increase in the doping concentration, that is a degree of oxidation, the length of the *c* axis shows a slight decrease, while the cell parameters, *a* and *b*, depend little on *x*. The chloride ions are located in the 1D channels between the LiPc columns, and the ion size (3.34 Å) is smaller than the channel diameter (*ca*. 4 Å). Therefore, the steric hindrance of the dopant molecules hardly affects the transverse direction of the LiPc molecules (red dots in Fig. 4.7). In contrast, there was a significant change in intermolecular interactions between molecular planes (blue dots in Fig. 4.7). In the 1D stacking array of LiPc before doping, each LiPc molecule has one unpaired electron, so that a Coulomb repulsive force works

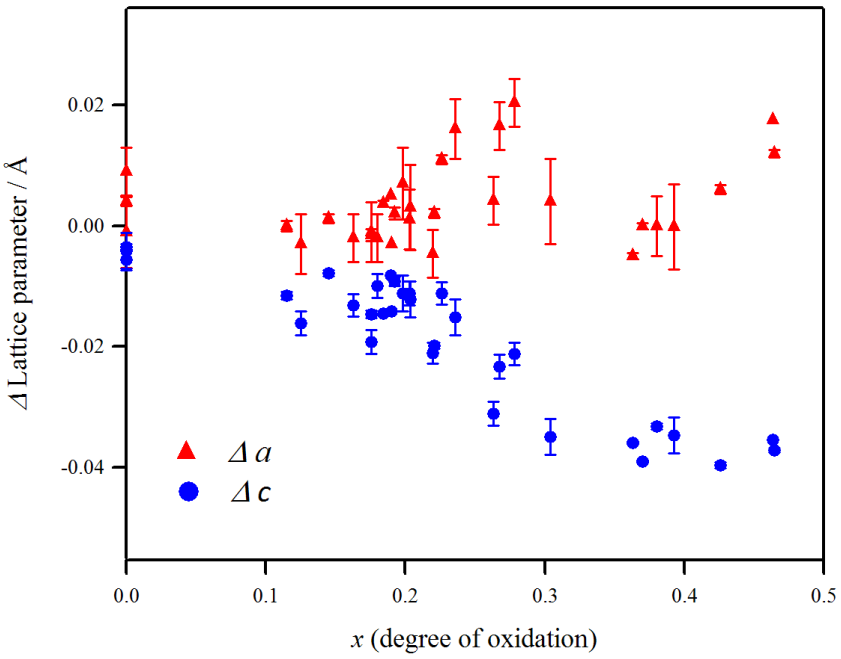

Figure 4.7 Evolution of the lattice constants *a* and *c* as a function of the Cl doping concentration.

between the molecules; the ground stat of the neutral LiPc can be regarded as a Mott insulator. Since such a Coulomb interaction becomes weaker as the density of the unpaired electrons decreases by the doping, the observed shrinkage along the *c* axis is considered to reflect an effective reduction of the Coulomb force.

4.5 Electrical Conductivity of $LiPcCl_x$ Crystals

The electrical conductivity was measured on the selected $LiPcCl_x$ crystals, listed in Table 4.1, with a two-probe technique. Gold wires were attached to the crystal by using a gold paste, and dc conductivity was measured parallel to the long axis of crystal which corresponds to the stacking axis of LiPc molecules (*c* axis).[10] Conductivity measurements were performed under vacuum and the sample temperature was monitored by a thermocouple adjacent to the crystal.

Fig. 4.8(a) shows the temperature dependence of conductivities for the $LiPcCl_x$ single crystals with various Cl concentrations, as well as pristine LiPc. The conductivity of the pristine LiPc crystal is 7×10^{-3} S cm^{-1} at room temperature, which agrees with the value, reported elsewhere.[11] Although the conductivity of thin films depends significantly on the crystallinity in the films,[11,12] such measurements based on single crystals can give more reproducible results.

It is shown that all the $LiPcCl_x$ crystals exhibit a semiconducting behavior with thermally activated conductivity. Fig. 4.8(b) and 4.8(c) show the conductivity at room temperature σ_{RT} and the Arrhenius activation energy E_a, respectively, for the $LiPcCl_x$ crystals, as a function of x. The conductivity of the $LiPcCl_x$ crystals, shows an continuous increase with Cl doping from $x = 0$ to 0.23. The electrochemical oxidation

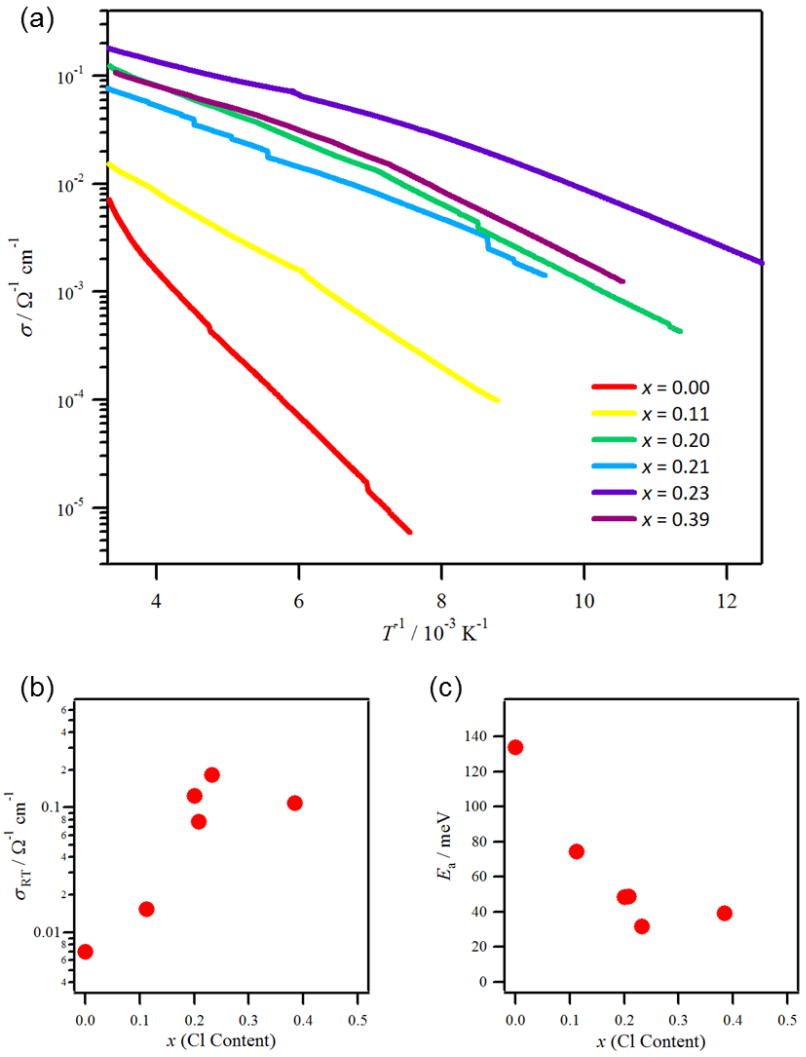

Figure 4.8 Temperature dependence of conductivities (a), Conductivities at room temperature σ_{RT} as a function of Cl concentration (b), and Arrhenius activation energy E_a as a function of Cl concentration (c) for $LiPcCl_x$ single crystals with various Cl concentrations as well as a pristine LiPc crystal.

removes some electrons from the SOMOs of LiPc arrays. This change is considered to result in not a decrease of a carrier density, but an effective decrease in the intersite Coulomb interactions. This is supported by the lattice shrink along the stacking axis, found in the range of $0 < x < 0.3$ for the Cl doping, as shown in Fig. 4.7. Namely, the

π-orbital overlap between neighboring molecules in the LiPc column becomes large, with enhancements of transfer integral and conductivity. In the range of $0.3 < x < 0.5$, the intermolecular spacing along the stacking axis was nearly constant in spite of the further Cl doping. This is probably the reason why the conductivity for the crystal with $x = 0.39$ is very similar to that for $x = 0.23$ (Fig. 4.8(b)). Although there have been no reports on a conductivity of LiPcCl, it is known that fully oxidized LiPcI,[13] which is isomorphous ($c/2 = 3.198$ Å) to the x-form LiPc[6] and NiPcI,[14] exhibit a relatively high conductivity of 0.2 S cm^{-1}. This value is similar to that for the LiPcCl$_x$ crystal with $x =$ 0.2–0.4. The activation energies of the LiPcCl$_x$ crystals depend on the x value, as shown in Fig. 4.8(c). The E_a is initially *ca*. 0.13 eV at $x = 0$, and then it gradually decreases to 0.03 eV, showing a saturation after $x \sim 0.3$.

Although obvious metallic behavior was not observed for LiPcCl$_x$ with $0 < x <$ 0.5, the conductivity increased by two orders of the magnitude, and the activation energy became 1/4 less than the original LiPc crystal due to the successful doping, maintaining their isomorphous structure. These results indicate a successful electrochemical doping for the LiPc crystals.

Fig. 4.9 shows the EPR intensity plot as a function of temperature for LiPcCl$_x$ with various dopant concentrations. The EPR signal intensities (χ_{EPR}) were normalized by that of a non-doped LiPc crystal at 300 K. The magnetic susceptibility of neat LiPc is known to be suppressed due to a cancellation between the spins of neighboring LiPc moelcules.[15] Fig. 4.9 indicates a further decrease in intensity over the whole temperature range. The electronic structure of the neutral LiPc can be regarded as a Mott state. The present data means that the decrease in the band filling from the half-filled state with an antiferromagnetic coupling decreases the susceptibility significantly.

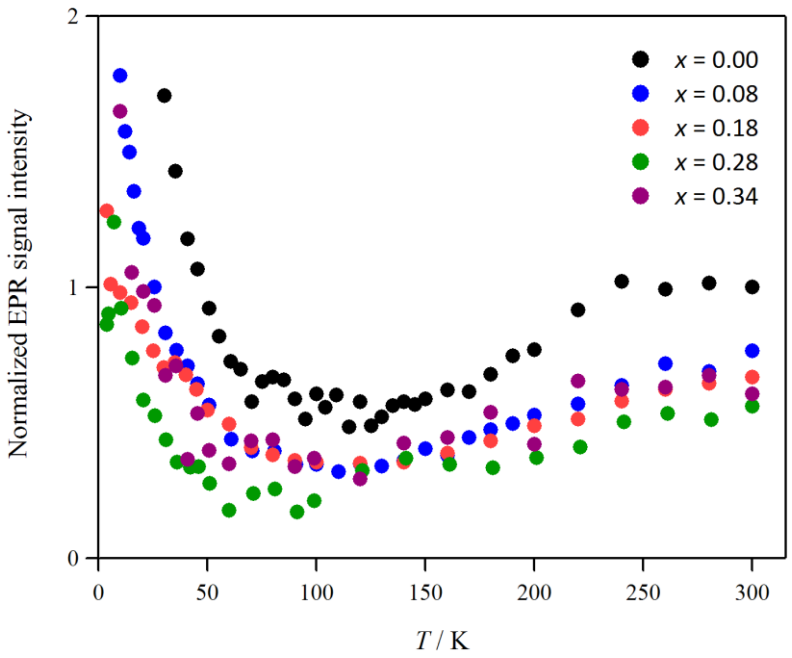

Figure 4.9 Temperature dependence of EPR signal intensities for selected single crystals of $LiPcCl_x$. The EPR signal intensities were normalized by that of non-doped LiPc crystal at 300 K.

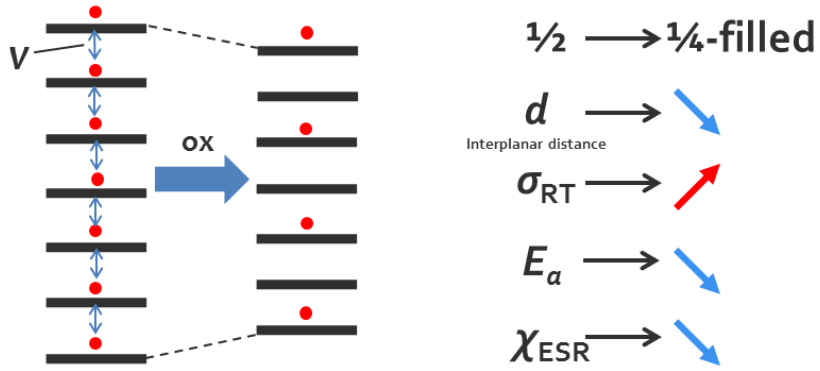

Figure 4.10 Schematic illustration of an effect of the oxidative doping to the π stacking in LiPc (left), and the various physical parameters (right).

4.6 Conclusion

Electrochemical doping to the single crystals of LiPc was carried out by a successive electrochemical method: the electrochemical growth of the single crystals of

LiPc, followed by their electrochemical oxidation in TBACl/acetonitrile solution. EDX and X-ray single crystal analyses confirmed that electrochemically doped LiPc crystals including Cl ions as counter anions, $LiPcCl_x$ were obtained with the value of x ranging from 0.1 to 0.5. X-ray single crystal analyses also exhibited that all of $LiPcCl_x$ crystals with different doping levels have isomorphous x-form structures, in which chloride ions with a relatively large thermal factor due to their disorder are located in the 1D channel formed between LiPc molecules. As the amount of the Cl dopant increases, the length of only the *c* axis became shorter, indicating that the π–π interactions between LiPc molecules along the *c* axis are improved (Fig. 4.10). Electrical measurements on $LiPcCl_x$ single crystals suggest a continuous enhancement of conductivity by a decrease in carrier number from the half-filled band as the Cl concentration increases. In other words, the structure and physical properties of neutral LiPc is considered to be governed by an electron correlation between the unpaired electrons. This is a good hint to understand the Mott states of molecular crystals.

References

1. G. Ilangovan, J. L. Zweier, P. Kuppusamy, Angew. *J. Phys. Chem. B* **2000**, *104*, 4047–4059.
2. K. Sakthivel, N. Munichandraiah, L. G. Scanlon, *J. Electrochem. Soc*. **2005**, *152*, C756–C763.
3. T. Laaksonen, V. Ruiz, L. Mutomäki, B. M. Quinn, *J. Am. Chem. Soc*. **2007**, *129*, 7732–7733.
4. G. M. Sheldrick, SHELXS-97: Program for crystal structure solution, University of Göttingen (Germany), **1997**.

5. G. M. Sheldrick, SHELXL-97: Program for crystal structure refinement, University of Göttingen (Germany), **1997**.
6. H. Sugimoto, M. Mori, H. Masuda, T. Taga, *J. Chem. Soc., Chem. Commun*. **1986**, 962–963.
7. B. N. Diel, T. Inabe, J. W. Lyding, K. F. Schoch, Jr., C. R. Kannewurf, T. J. Marks, *J. Am. Chem. Soc*. **1983**, *105*, 1551–1567.
8. C. J. Schramm, R. P. Scaringe, D. R. Stojakovic, B. M. Hoffman, J. A. Ibers, T. J. Marks, *J. Am. Chem. Soc*. **1980**, *102*, 6702–6713.
9. J. G. Gaudiello, G. E. Kellogg, S. M. Tetrick, T. J. Marks, *J. Am. Chem. Soc*. **1989**, *111*, 5259–5271.
10. M. Brinkmann, J.-J. Andre, *J. Mater. Chem*. **1999**, *9*, 1511–1520.
11. P. Petit, P. Turek, J.-J. Andre, R. Even, J. Simon, R. Madru, M. A. Sadoun, G. Guillaud, M. Maitrot, *Synth. Met*. **1989**, *29*, F59–F64.
12. P. Turek, P. Petit, J.-J. Andre, J. Simon, R. Even, B. Boudjema, G. Guillaud, M. Maitrot, *J. Am. Chem. Soc*. **1987**, *109*, 5119–5122.
13. M. Dumm, P. Lunkenheimer, A. Loidl, B. Assmann, H. Homborg, P. Fulde, *J. Phys. Chem*. **1996**, *104*, 5048–5053.
14. C. J. Schramm, R. P. Scaringe, D. R. Stojakovic, B. M. Hoffman, J. A. Ibers, T. J. Marks, *J. Am. Chem. Soc*. **1980**, *102*, 6702–6713.
15. M. Brinkmann, J.-J. Andre, *J. Mater. Chem*. **1998**, *8*, 675–685.

Chapter 5. Summary

In this thesis, electrochemical doping has been applied to organic thin films and crystals for the purpose to modulate the physical properties of organic compounds by controlling the band-filling while maintaining the band structure. In order to avoid a deformation of their crystal and thin film structures, which is usually caused by a penetration of counter ions during electrochemical doping, this study focused on porphyrazines such as tetrakis(thiadiazole)porphyrazine (H_2TTDPz) and lithium phthalocyanine (LiPc), taking advantage of their robust structures.

In Chapter 2, the electrochemical doping of the H_2TTDPz thin film was investigated. H_2TTDPz thin films prepared by vacuum vapor deposition exhibited a high and unusual orientation of the molecular planes; the planes are all parallel to the substrate surface. As the photocurrent and FET characteristics of H_2TTDPz thin film revealed *n*-type behavior, the electrochemical reduction of H_2TTDPz thin film was observed in the cyclic voltammetry in NH_4Cl aqueous solution, reflecting a high electron affinity of *n*-type semiconductor. This electrochemical doping with nearly one electron occurs accompanied by electrochromism, and enhanced intermolecular interactions were indicated by the presence of charge-transfer band and the enhancement of electrical conductivity. Their robust structure was supported by the XRD patterns which exhibited that the lamellar structure of H_2TTDPz still remained even after the penetration of counter ions.

In Chapter 3, the electrochemical doping of the LiPc thin film was investigated. The pristine α-form thin films of LiPc exhibited a structural transformation to the x-form by electrochemical oxidation which introduces the counter anions (ClO_4^-) into

the thin films, and these anions are reversibly dedoped by electrochemical re-reduction, maintaining the x-form structure. Electrical resistivity measurements on the LiPc thin films by electrochemical doping demonstrated that all the doped LiPc thin films exhibited lower resistivity by 2-3 orders of magnitude than the pristine film.

In Chapter 4, the electrochemical doping of LiPc was developed into advanced study with single-crystalline LiPc. The electrochemical oxidation of LiPc crystals in TBACl/acetonitrile solution gave the isomorphous Cl-doped LiPc crystals ($LiPcCl_x$). Various dopant concentrations were realized in the range from 0 to 0.5, although the maximum *x* value was limited below 0.5 due to the decomposition of the electrolyte. As a result of X-ray single crystal structure analyses, the length of LiPc stacking axis was found to become shorter as the *x* value increased, indicating the improved interplanar interactions in LiPc stacks, in contrast to no significant change in the *a* and *b* axis length. Accordingly, the dc conductivity of $LiPcCl_x$ was enhanced as the dopant concentration increased, and showed a relatively high conductivity of $\sigma_{RT} = 0.2$ S cm^{-1}. The structure and physical properties of neutral LiPc is therefore considered to be governed by an electron correlation between the unpaired electrons.

In conclusion, the electrochemical doping was successfully carried out on thin films and crystals of porphyrazines such as H_2TTDPz and LiPc. As a result of band-filling control by the electrochemical doping, their conductivities were significantly enhanced. These results suggest that a strong intermolecular interaction such as π–π interactions, electrostatic interactions, etc. and a porous structure are crucial factors for electrochemical doping while maintaining crystal and thin film structures. Especially, a porous structure seems to have the biggest potential for an ideal band-filling control, since adsorption/desorption of counter ions into/from crystals and

thin films are reversible without deformation of their structures. This means that porous materials such as metal-organic-frameworks (MOFs) are good candidates, and the electrochemical doping would be applicable to control not only an electrical conductivity, but also a magnetic, optical, catalytic, and other physical properties.

Acknowledgements

The work in this thesis has been carried out under the supervision of Professor Kunio Awaga, Research Center for Materials Science, Nagoya University.

The author wishes to express his sincere gratitude to Professor Kunio Awaga for his kind guidance, valuable discussion and continuous encouragement throughout the work. The author is deeply grateful to Assistant Professor Hirofumi Yoshikawa and Associate Professor Michio M. Matsushita, for their helpful suggestion and selfless help in the experimental work.

The author wishes to thank Associate Professor Hiroshi Ito of Department of Applied Physics, Nagoya University for his selfless help and helpful discussion in the work of photoconductivity of H_2TTDPz thin films. The author is grateful to Professor Toshihiko Yokoyama of Institute for Molecular Science for his great help and helpful discussion on XPS measurements.

The author wishes to thank all lab members in Awaga group for their kind support in his research and fruitful discussion.

This work was supported by Grant-in-Aid for JSPS Fellows. A part of this Ph.D. thesis was done in the IRTG program between Nagoya University and University of Münster (Germany). The author also would like to thank my IRTG supervisor, Professor Hellmut Eckert of University of Münster for his kind guidance and invaluable discussion, and Dr. J. Ren of University of Münster and Ms. Z. Zeng for their kind assistance on NMR measurements.

Finally, the author sincerely thanks his parent for their continuous moral supports.